ABSTRACT

Title of Dissertation: The Development of Tunnel Diode Oscillators And
High Magnetic Field Studies of
Unconventional Superconductor UTe_2:
Unveiling the Phase Diagram And
Unconventional Hall Effect

Wen-Chen Lin
Doctor of Philosophy, 2023

Dissertation Directed by: Professor Johnpierre Paglione
Department of Physics

This dissertation presents an extensive investigation of UTe_2 under various magnetic field and pressure conditions by utilizing the Tunnel Diode Oscillator (TDO) and electrical transport. The study is primarily divided into three parts.

The first part focuses on the utilization of the TDO to establish a magnetic susceptibility measurement device. The TDO's frequency, highly sensitive to inductance changes due to the negative I-V curve regime of the tunnel diode, is harnessed to create a measurement circuit compatible with low-temperature refrigerators. The design and development process of these devices are thoroughly detailed.

The second part unveils the comprehensive (H, T, P) phase diagram of UTe_2 under magnetic fields reaching 41 T along the crystallographic b-axis, combined with applied pressures of up to 18.8 kbar. Utilizing magnetoresistance and tunnel diode oscillator measurements, we investigated

the pressure-induced evolutions of multiple phases. By monitoring the field-induced transition between superconducting and magnetic field-polarized phases across various pressures (up to 18.8 kbar), we track the suppression of this transition with increasing pressure. This suppression culminates in the disappearance of superconductivity near 16 kbar, concurrently leading to a distinct, pressure-induced magnetic ordered state that is stable at zero field. The evolution of a second superconducting phase and its upper critical field under pressure are also investigated, leading to insights into the confinement of superconductivity by magnetic phases and the boundaries of triplet superconductivity.

The third part uncovers an unconventional Hall effect in UTe_2 induced by an in-plane magnetic field, in accordance with recent observations in nonmagnetic VS-VS_2 superlattice materials and $ZrTe_5$. An extensive study was conducted on the field and angle dependence of the Hall response under in-plane fields, confirming its field-odd symmetry nature, which aligns with the recently identified in-plane Hall effect. We examined the field dependence of the Hall response up to 33 T, and observed a remarkable enhancement, indicating a significant linkage to the well-identified metamagnetic transition. In addition, we will discuss the symmetry restrictions on the in-plane Hall response, and evidence of symmetry lowering in our system.

The Development of Tunnel Diode Oscillators And High Magnetic Field Studies of Unconventional Superconductor UTe_2: Unveiling the Phase Diagram And Unconventional Hall Effect

by

Wen-Chen Lin

Dissertation submitted to the Faculty of the Graduate School of the
University of Maryland, College Park in partial fulfillment
of the requirements for the degree of
Doctor of Philosophy
2023

Advisory Committee:
  Professor Johnpierre Paglione, Chair/Advisor
  Professor Steven Anlage
  Professor Nicholas Butch
  Professor Ouyang Min
  Professor Efrain Rodriguez, Deans Representative

Foreword

The following is a list of all the papers that I have contributed to during my time as a graduate student, either published or intended for publication, starting with the most recent. Those whose results are covered extensively in this thesis are marked with an asterisk.

*Y.S. Eo, **W.-C. Lin**, S. Ran, S. Saha, D. Graf, N.P. Butch, and J Paglione, ”In-plane Hall Effect in UTe_2”, in preparation.

***W.-C. Lin**, D.J. Campbell, S. Ran, I-L. Liu, H. Kim, A.H. Nevidomskyy, D. Graf, N.P. Butch, J. Paglione, ”Tuning Magnetic Confinement of Spin-triplet Superconductivity”, NPJ Quantum Materials **5**, 68 (2020).

H. Hodovanets, C.J. Eckberg, P.Y. Zavalij, H. Kim, **W.-C. Lin**, M. Zic, D.J. Campbell, J.S. Higgins, J. Paglione, ”Single-crystal Investigation of the Proposed Type-II Weyl Semimetal CeAlGe”, Phys. Rev. B **98**, 245132 (2018).

Acknowledgments

My deepest gratitude goes first and foremost to my advisor, Johnpierre Paglione. His unwavering support, invaluable guidance, and steady encouragement have been crucial to my work. As the head of a top-notch research team, he provided me with an excellent research environment that enriched my studies. But his support didn't stop there; during my pregnancy and the early stages of raising my baby, his understanding and assistance were invaluable. For his blend of professional guidance and personal kindness, I am truly thankful.

Thanks should also go to Prof. Nicholas Butch, Prof. Steven Anlage, Prof. Min Ouyang, and Prof. Efrain E. Rodriguez for their invaluable input as members of my thesis committee and their time dedicated to reviewing my manuscript.

I would like to extend my sincere thanks to Hyunsoo Kim, whose initial guidance set the foundation for my research journey. I appreciate his guidance in developing tunnel diode oscillator devices. Moreover, I learned how to be a researcher from him, including but not limited to research skills and professional knowledge. Special thanks to Yun Suk Eo, who initiated the Hall Effect project. I'm grateful to work on this project with him. Besides, he spent valuable time reviewing my manuscript and providing helpful suggestions.

I extend heartfelt thanks to Daniel Campbell and Sheng Ran, who contributed to these projects. I want to thank my group members, especially those who helped with my research, Halyna Hodovanets, Shanta Saha, Hyeok Yoon, Tristin Metz, Jarryd Horn, I-Lin Liu, Ian Hayes, and Ryan Dorman. Also, I had the pleasure of working with Chris Eckberg, Prathum Saraf, John Collini, Rahul Sharma, Kefeng Wang, Limin Wang, Connor Roncaioli, Atsutoshi Ikeda, Sylvia Lewin, Keenan Avers, Corey Frank, Dan Sokratov, Emerson Hemley, Yash Anand, Winslow Weiss, Alonso Suarez, Mark Zic, Brandon Wilfong. Thanks for the support and discussions.

I also want to thank the people at QMC, Josh Higgins, Douglas M. Bensen, and Brian Straughn, who helped my research by providing technical support.

External collaborators were crucial to this work, and for that, I express my gratitude to David Graf from NHMFL for his significant assistance with high magnetic field experiments. Prof. Andriy Nevidomskyy also deserves special mention for his theoretical insights that clarified my experimental results.

Lastly, I must thank my family. Thanks to my parents for their love and support throughout my life. Thanks to my husband, Huan-Kuang Wu, for supporting me at my worst and inspiring me to do my best. To my sweet daughter, Nora, thank you for bringing joy and light into my life.

Table of Contents

List of Tables

List of Figures

List of Abbreviations

AHE	anomalous Hall effect
BCS	Bardeen, Coper and Schrieffer
FP (phase)	field-polarized (phase), see Fig. 3.8
GL	Ginzburg-Landau
INS	inelastic neutron scattering
IPHE	in-plane Hall effect
IV	current-voltage
NHMFL	National High Magnetic Field Laboratory
N (phase)	normal (phase), see Fig. 3.8
MO (phase)	magnetic-ordered (phase), see Fig. 3.8
MR	magnetoresistance
OPHE	out-of-plane Hall effect
PPMS	Physical Property Measurement System
SC1 (phase)	first superconducting (phase), see Fig. 3.8
SC2 (phase)	second superconducting (phase), see Fig. 3.8
TDO	tunnel diode oscillator
VTI	Various Temperature Insert
WHH	Werthamer, Helfand, and Hohenberg
λ	penetration depth
ξ	Ginzburg-Landau coherence length
Δ	superconducting gap

ψ	superconducting order parameter
Φ_0	magnetic flux quantum
χ	magnetic susceptibility
κ	Ginzburg-Landau parameter
T_c	superconducting critical temperature
$T_{c(2)}$	superconducting critical temperature of the SC1 phase
T_{Curie}	Curie temperature
T_M	temperature corresponds to the local maximum of R(T), see the inset of Fig. 3.8 (d)
H_c	thermodynamic critical field
H_{c2}	upper critical field
$H_{c2(2)}$	upper critical field of the SC2 phase
H^*	cutoff field where the SC1 phase truncated by the FP phase, see Fig. 3.4 (b)
H_{FP}	field corresponds to the crossover to the FP phase, see Fig. 3.6 (e)
H_p	field corresponds to the peak of resistance, see Fig. 3.4 (b)
H_{hy}	field where the demise of hysteresis in resistance

Chapter 1: Introduction

1.1 An Overview of Conventional Superconductivity

Superconductivity is a material property characterized by zero DC electrical resistance and perfect diamagnetism when cooled below the critical temperature (T_c). Historically, the discovery of superconductivity was made by Onnes in 1911 on solid mercury, where the electrical resistance abruptly vanishes below 4.2K [1]. In 1933, the Meissner effect, which is the phenomenon of superconductors expelling applied magnetic fields, was discovered by Meissner and Ochsenfeld [2].

On the theory side, the London equation [3] was the first to explain the Meissner effect, predicting an exponential decay profile of the penetrated magnetic field into the superconductor with the penetration depth

$$\lambda = \sqrt{\frac{m}{\mu_0 n_s e^2}} \tag{1.1}$$

where n_s is the superconducting electron density by the two-fluid model.

A phenomenological model based on the second-order nature of the phase transition across T_c was later proposed by Ginzburg and Landau [4], where the free energy of the normal and superconducting states was written down in terms of the order parameter. Upon including magnetic field and spatial fluctuation of the order parameter, Ginzburg-Landau (GL) theory correctly captures the physics at the critical magnetic field, where the superconductor breaks down. Additionally, it introduced another length scale of superconductors, the Ginzburg-Landau coherence length

$$\xi = \frac{\hbar^2}{\sqrt{2m_*|\alpha|}} \tag{1.2}$$

where α is a phenomenological parameter and ξ is the length scale at which the order parameter is restored from a defect. The ratio between the two length scales is the so-called Ginzburg-Landau parameter $\kappa = \frac{\lambda}{\xi}$.

Ginzburg and Landau were able to predict two classes of superconductors depending on the order of phase transition across the phase boundary in the magnetic field. Namely, it could be either an abrupt phase transition (1st order) or a continuous one (2nd order). This idea was made clear by Abrikosov [5], where he found that in the regime that $\kappa > \frac{1}{\sqrt{2}}$, the superconductor supports the formation of vortices of magnetic flux. As the magnetic field increases, the number of vortices increases, ultimately forming a 2D triangular lattice. In this case, the transition is a second-order phase transition, and this class of superconductors is called type-II superconductor.

In 1957, Bardeen, Cooper, and Schrieffer (BCS) produced the first microscopic theory of superconductivity (BCS theory) [6]. This groundbreaking work is composed of three major insights: Cooper instability, the effective attractive potential near the fermi surface, and a coherent many-body ground state.

Due to the high electron density and screening, the normal state of a usual metal can be well approximated by the Fermi-sea state. It was demonstrated by Cooper that upon a weak attractive interaction, the Fermi-sea state is unstable against the formation of bound states of paired electrons, an effect now known as Cooper pairing. The Cooper pairs are composed of electrons around the Fermi level with opposite spin and momentum.

The crucial ingredient is an attractive electron-electron interaction that can overcome the Coulomb repulsion around the Fermi surface. Bardeen considered the phonon mediated electron-electron interaction that arises in the second order expansion of the electron-phonon interaction. Using the jellium model with the Thomas-Fermi screening mechanism, the effective interaction shows an attractive window close to the Fermi level.

Finally, Schrieffer was able to write down the many-body wave function of the superconductor

$$|\psi\rangle = \prod_k (u_k + v_k c^\dagger_{k\uparrow} c^\dagger_{-k\downarrow})|0\rangle \tag{1.3}$$

where $|v_k|^2$ corresponds to the probability that the two states, $|k, \uparrow\rangle$ and $|-k, \downarrow\rangle$, being occupied and $|u_k|^2 + |v_k|^2 = 1$. The Schrieffer state can be interpreted as a coherent state of paired electrons. The key property here is that there exists a phase for $\frac{v_k}{u_k}$ which is universal for all Cooper pairs of different momentum. This universal phase relates to the breakdown of U(1), giving rise to the Meissner effect.

Multiple predictions of BCS theory showed excellent agreement with experiment, including the famous energy gap equation at $T \ll T_c$,

$$E_g = 3.528kT_c \tag{1.4}$$

By considering the aa-phonon interaction, it also correctly predicted the isotope effect measured in the experiments,

$$T_c \propto M^{-\alpha} \tag{1.5}$$

where M is the isotopic mass and $\alpha = \frac{1}{2}$ by BCS theory, which is in excellent agreement with ordinary superconductors. This solved the mystery of conventional superconductivity that lasted two decades and was awarded the Nobel prize in 1972.

1.2 Upper Critical Field of Type-II Superconductors

The upper critical field, or H_{c2}, is the magnetic field at which a superconductor is transformed from the Abrikosov state to the normal state and the superconductivity is completely suppressed. This phase transition can be understood as the competition between different sources of magnetic energy and the pairing energy of superconductivity. There are two main mechanisms for the breakdown of superconductivity under magnetic field: the orbital pair-breaking effect and the paramagnetic pair-breaking effect.

For the orbital pair-breaking effect, we will start with the GL theory, which captures the physics close to T_c. Through minimization of the GL free energy, one obtains the GL equation of the spatial-dependent superconducting order parameter ψ,

$$\left[-\frac{\hbar^2}{2m_*}\left(\nabla + \frac{2ei}{\hbar}A\right)^2 + \alpha + \beta|\psi|^2\right]\psi = 0 \tag{1.6}$$

where α and β are the phenomenological parameters and m_* is the effective mass of electron. Due to the second order nature, close to the phase transition, we can assume $|\psi|^2 \to 0$ and drop the nonlinear term. As a result, the GL equation becomes formally equivalent to the quantum Hall problem, under the Landau Gauge, the eigenvalue problem becomes

$$\left(n + \frac{1}{2}\right)\hbar\omega_c + e_{kz} = |\alpha| \tag{1.7}$$

where ω_c is the cyclotron frequency $\frac{2eB}{m^*}$ and e_{kz} is the kinetic energy in the z direction $\frac{\hbar^2 k_z^2}{2m^*}$. In this context, H_{c2} appears as the magnetic field above which there is no solution to the GL equation, corresponding to $n, e_{kz} = 0$, or

$$H_{c2} = \frac{\Phi_0}{2\pi\mu_0\xi^2} \tag{1.8}$$

In terms of the thermodynamic critical field $H_c = \frac{\Phi_0}{2\pi\mu_0\sqrt{2}\xi\lambda}$ at which the free energy gain from condensation is overcome by the magnetic field energy. We have the important result

$$H_{c2} = \sqrt{2}\kappa H_c \tag{1.9}$$

Accordingly, at $\kappa > \frac{1}{\sqrt{2}}$, H_{c2} becomes greater than H_c, thus opening the window for a second order phase transition.

The more accurate theory for orbital-pair breaking is presented by Werthamer, Helfand, and Hohenberg (WHH) [8]. They solved the Gorkov self-consistent equation for superconductivity, which employed the Green's function formalism and incorporates the microscopic BCS equation with the effect of impurities. Note that only the orbital effect of the magnetic field is considered in the Gorkov equations. In its unitless form, the zero-temperature upper critical field and its slope at T_c takes a universal linear relation,

$$H_{c2}^{WHH}\big(T=0\big) \approx -0.693 \frac{dH_{c2}}{dT}\bigg|_{T=T_c} T_c \tag{1.10}$$

This widely used form is applied to predict the $H_{c2}(0)$ in many experiments and its temperature dependence is shown in Fig. 1.1.

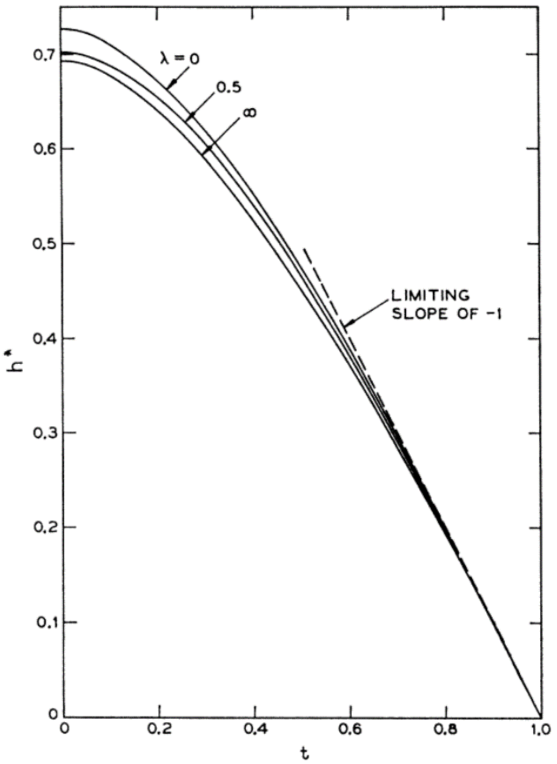

Figure 1.1: The reduced upper critical field $h^* = -H_{c2}(T)/\left.\frac{dH_{c2}}{dT}\right|_{T=T_c}$ vs. reduced temperature $t = T/T_c$ calculated by Werthamer, Helfand, and Hohenberg [7]. Different purities are considered where $\lambda = 0$ and $\lambda = \infty$ correspond to the clean and dirty limits, respectively.

In addition to the orbital degree of freedom, the magnetic field also interacts with electron spins. Under an external magnetic field, the electrons in the normal state of a paramagnetic metal will be polarized towards the direction of the field. This is due to the Zeeman effect, with the energy term $E_Z \approx -\vec{B} \cdot \vec{s}$. In a conventional superconductor, on the other hand, such an effect will suppress superconductivity whose Cooper pairs are in the spin singlet state which exhibits a higher Zeeman energy compared to the polarized state. At the Pauli limit H_P, the polarization energy becomes equal to the condensation energy of Cooper pairs, or

$$\frac{1}{2}\chi_n H_p^2 = \frac{1}{2}N(0)\Delta \tag{1.11}$$

where χ_n is the normal state susceptibility given by $g^2\mu_B^2 N(0)/2$, $N(0)$ is the density of states at the Fermi level and Δ is the superconducting energy gap. Then, the Pauli limit H_p is

$$\mu_0 H_p = \alpha T_c \tag{1.12}$$

where $\alpha = 1.84$ Tesla/Kelvin.

Unlike the orbital pair-breaking effect, a pure paramagnetic pair-breaking transition is first order, where the transition is discontinuous. In real material, both the orbital and paramagnetic pair-breaking effect will contribute to the upper critical field, restoring back the second order nature of the phase transition [9].

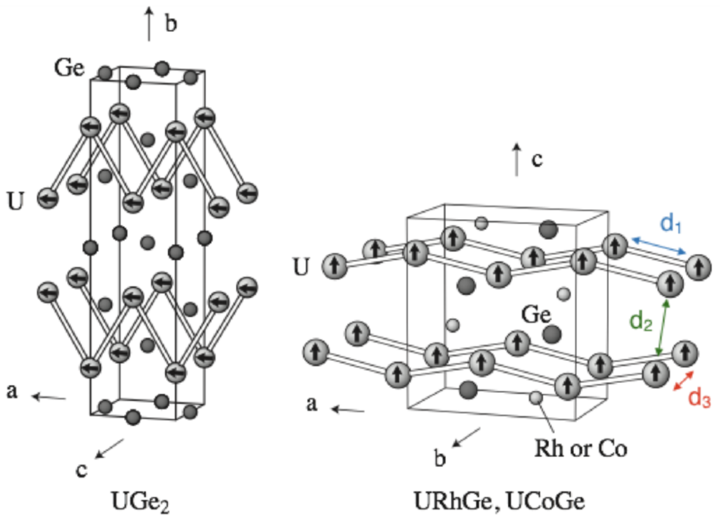

Figure 1.2: The crystal structure of (a) $\mathrm{UGe_2}$, (b) URhGe and UCoGe [12].

1.3 Uranium-Based Superconductors

In the 2000s, superconductivity was discovered in uranium-based ferromagnetic compounds, initially in UGe_2 under applied pressure [**?**]. Subsequently, superconductivity was observed in URhGe [10] and UCoGe [11] at ambient pressure. Among these materials, UGe_2 exhibits the most robust ferromagnetism with $T_{Curie} = 52\,K$ but the weakest superconductivity, only present under pressures ranging from 1.1 GPa to 1.6 GPa. Conversely, UCoGe has the weakest ferromagnetism with $T_{Curie} = 2.7K$ but the strongest superconductivity with 0.8 K T_c at ambient pressure.

The crystal structures of some uranium-based superconductors are shown in Fig. 1.2. All three compounds exhibit an orthorhombic structure. UGe_2 belongs to the Cmmm space group, while URhGe and UCoGe are in the Pnma space group. In each compound, uranium atoms create zigzag chains along the a-axis. The magnetic easy axis aligns with the a-axis for UGe_2 and the

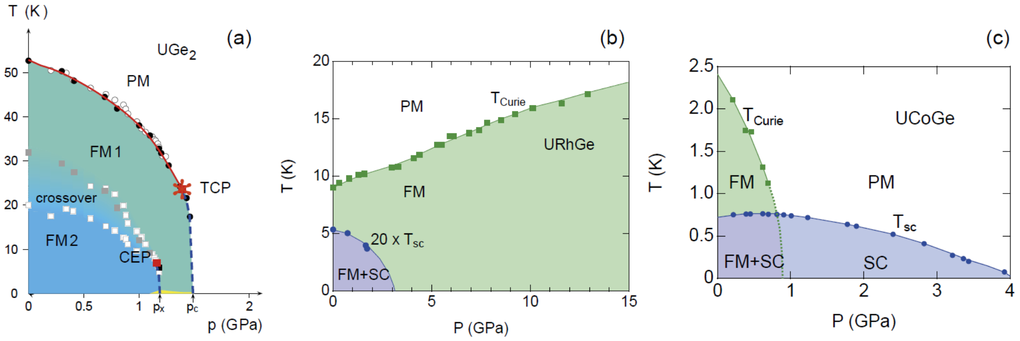

Figure 1.3: The temperatrue-pressure phase diagrams of (a) $\mathrm{UGe_2}$, (b) URhGe and (c) UCoGe [13].

c-axis for URhGe and UCoGe.

The uranium-based ferromagnetic superconductors exhibit rich phase diagrams, illustrating the interplay between superconductivity and ferromagnetism (Fig. 1.3). In URhGe and UCoGe, superconductivity and ferromagnetism coexist, suggesting spin-triplet pairing. Superconductivity appears to be strengthened by significant ferromagnetic fluctuations at the ferromagnetic phase boundaries [14, 15]. In $\mathrm{UGe_2}$ and UCoGe, the superconducting dome is centered around the ferromagnetic phase boundaries. In URhGe, the pressure-driven evolution of the Curie temperature and the critical temperature displays an inverse relationship, indicating that superconductivity weakens as it deeps into the ferromagnetic phases.

In striking contrast to conventional superconductors, where the superconducting state breaks above the critical field, applying a magnetic field in specific directions can boost superconductivity in uranium-based ferromagnetic compounds, as depicted in the H-T phase diagrams (Fig. 1.4). In $\mathrm{UGe_2}$, a magnetic field parallel to the magnetic easy axis (H||a) under certain pressure can cause a transition between two ferromagnetic phases. The ferromagnetic fluctuations around the

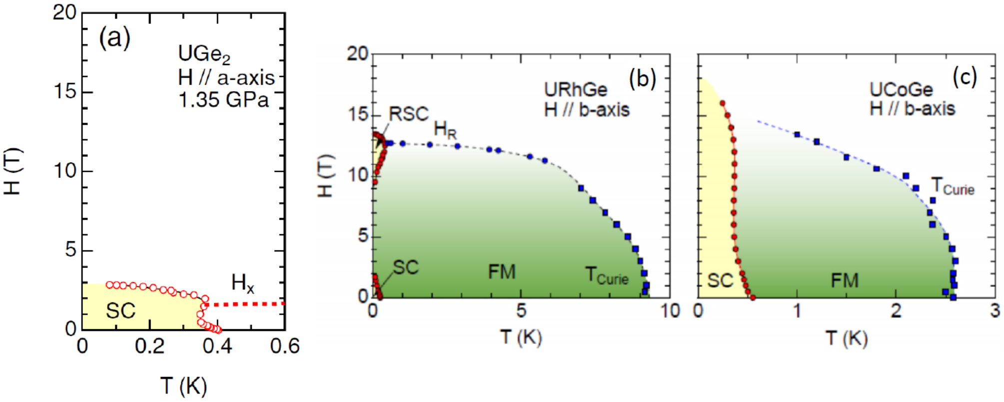

Figure 1.4: The field-temperature phase diagrams (a) UGe$_2$ [16], (b) URhGe [17] and (c) UCoGe [18]. The fields are along the directions that can induce reentrant superconductivity. Note that the UGe$_2$ phase diagram is at a pressure near the superconducting dome's center.

phase boundary stimulate superconductivity, resulting in field-enhanced superconductivity. In URhGe and UCoGe, reentrant superconductivities are induced by magnetic fields perpendicular to the easy axis. The transverse fields lead to the collapse of Ising ferromagnetism along the easy axis, generating ferromagnetic fluctuations that drive superconductivity. The alignment of the superconducting enhancements with the boundaries of the ferromagnetic phases also supports this view.

For a comprehensive review of uranium-based ferromagnetic superconductors, the reader is suggested to read [12].

1.4 UTe$_2$

In 2019, superconductivity in UTe$_2$ single crystals was discovered with a critical temperature of 1.6 K [19]. Distinct from uranium-based ferromagnetic superconductors, UTe$_2$ is paramagnetic

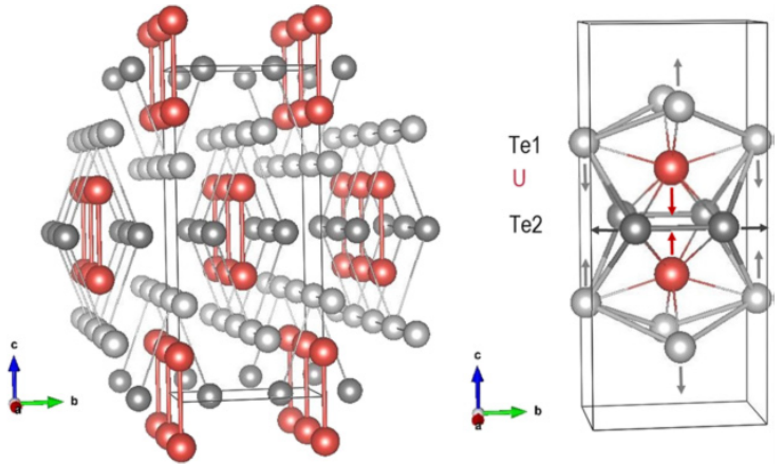

Figure 1.5: The crystal structure of UTe_2. The uranium ladders are colored red. [21].

and does not exhibit magnetic ordering even down to 50 mK [19]. UTe_2 has a body-centered orthorhombic crystal structure with Immm space group (No.71, D_{2h}^{25}) (Fig. 1.5). The uranium atoms form a two-leg ladder structure along the a-axis (the magnetic easy axis) with the rungs along the c-axis. The tellurium atoms, Te(1) and Te(2), are located at two different sites, and the Te(2) atoms form chains along the b-axis [20].

UTe_2 exhibits unique superconductivity properties. Firstly, the upper critical fields for all field directions are far above the Pauli limit, suggesting spin-triplet pairing [19]. When the field is along the b-axis, superconductivity endures under fields up to 35 T where a metamagnetic transition truncates the superconductivity [22]. Secondly, multiple superconducting phases exist under various field-temperature-pressure conditions [22, 23, 24, 25]. In Chapter 3, we will present the phase boundaries between two superconducting phases captured by tunnel diode oscillators. Lastly, UTe_2 displays intriguing properties in its reentrant superconductivity, such as coinciding phase boundary with the field-polarized phase and withstanding exceptionally high magnetic fields beyond 65 T, which is the limit of measurements [22].

UTe_2 is a promising candidate for an intrinsic topological superconductor which is an ideal platform for robust topological quantum computation [20]. This is supported by numerous observations. Spin-triplet pairing, a stepping stone for nontrivial topology, has been demonstrated in UTe_2 through various findings, such as an upper critical field exceeding the Pauli limit and a negligible Knight shift change near the critical temperature [26, 27]. Among unconventional superconductors, p-wave superconductors are capable of hosting Majorana fermions [28, 29], and UTe_2 is believed to have a nodal gap structure, consistent with p-wave symmetry, as suggested by thermal transport [30] and dielectric resonator surface impedance [31] measurements.

Additionally, a two-component order parameter and broken time-reversal symmetry are evidenced by double superconducting phase transitions in specific heat and the finite polar Kerr effect below T_c [32]. UTe_2's broken time-reversal symmetry indicates its potential as a Weyl superconductor. Furthermore, nontrivial band topology in UTe_2 is suggested by STM studies observing chiral surface state signatures [33].

Researchers have been seeking an intrinsic topological superconductor, but so far, only a few candidates have been identified, such as $\mathrm{Sr_2RuO_4}$ [34], $\mathrm{Au_2Pb}$ [35], and $\mathrm{TaIrTe_4}$ [36]. None of these have been confirmed as topological superconductors. Among current candidates, UTe_2 stands out as a strong contender, displaying intriguing properties that point toward topologically nontrivial possibilities.

The pairing mechanism of superconductivity in UTe_2 remains uncertain. For uranium-based ferromagnetic superconductors, superconductivity is thought to be driven by ferromagnetic fluctuations. However, as a paramagnetic superconductor, the presence of ferromagnetic fluctuations in UTe_2 is still a matter of debate. While magnetic-field-trained polar Kerr effect measurements suggest the existence of ferromagnetic fluctuations [37], inelastic neutron scattering (INS) experiments do not detect them. Instead, recent INS experiment reveals magnetic excitations obey paramagnetic symmetry, consistent with Kondo lattice phenomena with low-dimensional band structures [38]. On the other hand, photoemission measurements and band structure calculations propose a quasi-2D Fermi surface [39, 40, 41]. Consequently, it has been suggested that superconductivity under a magnetic field could be stabilized by the resonance between the magnetic field energy and the hopping energy of two conducting layers [42, 43].

Chapter 2: The Development of Tunnel Diode Oscillators for Low-Temperature Measurements

This chapter delves into the progression of the development of tunnel diode oscillators (TDO) intended for magnetic susceptibility measurements at low temperatures. All stages of development have taken place at the University of Maryland by me under the guidance of Dr. Hyunsoo Kim. The chapter will introduce TDO devices custom-tailored for different refrigeration systems, such as the Physical Property Measurement System, the Variable Temperature Insert, and the dilution refrigerator. Furthermore, an advanced TDO device, specifically designed to enhance the accuracy of temperature-dependent measurements, will also be introduced.

2.1 Overview of Tunnel Diode Oscillators

The tunnel diode oscillator (TDO) is an electronic circuit that generates a stable radio frequency oscillation with DC power [44]. The circuit is an LC oscillator driven by a tunnel diode, and the values of LC components determine the oscillation frequency, typically in the order of 1-100 MHz. A tunnel diode or Esaki diode is a heavily doped semiconductor diode. It is comprised of a pair of n-type and p-type semiconductors, like ordinary diodes. However, the impurities in both types of semiconductors in a tunnel diode are 1000 times greater than in the standard diode. The high impurity level causes a narrow depletion region about 10 nm

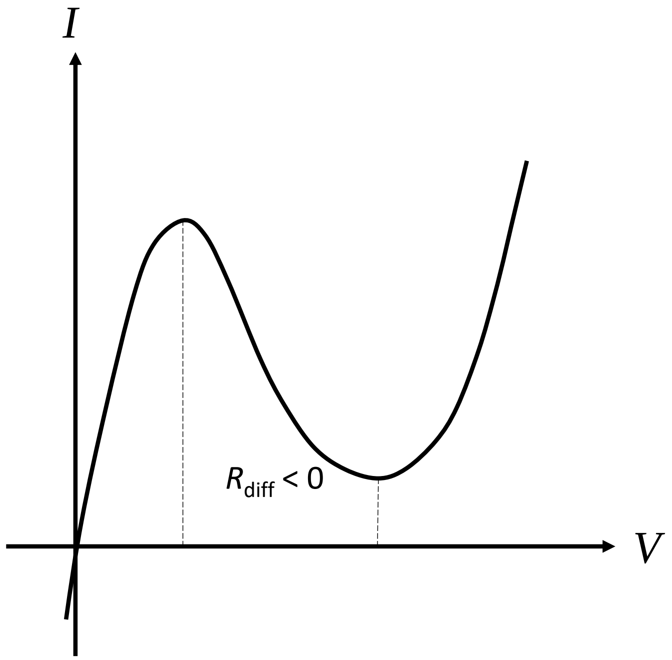

Figure 2.1: IV curve of tunnel diodes. The tunnel diode has negative differential resistance in the region between the dashed lines.

wide between the two semiconductors. The nanometer-scale depletion region allows electrons to tunnel through, giving rise to the tunneling current between two types of semiconductors.

The tunnel diode is characterized by its unique current-voltage relation. Unlike ordinary diodes, whose current-voltage (IV) curves are monotonically increasing, the IV curve of tunnel diodes looks similar to the shape of a cubic function, as shown in Fig. 2.1. The current decreases with increasing voltage in the region between the local maximum and the local minimum of the IV curve. In this region, the diode has negative differential resistance, which is the most crucial property of it for applications in oscillators, switches, and amplifiers.

The tunneling current between two types of semiconductors causes the unique IV property of tunnel diodes. To understand this effect, we need to look into the energy bands of tunnel diodes. As mentioned, a tunnel diode is comprised of n-type and p-type semiconductors. Due to the heavy doping, the conduction band of the n-type and the valence band of the p-type overlap. Under a forward bias, electrons tunnel through the narrow p-n junction barrier from the n-type conduction band to the p-type valence band, resulting in a nonzero tunneling current flow. As voltage increases slightly, the energy levels of the band edges move closer, so the tunneling current increases. When the two band edges align, the tunneling current reaches its maximum, creating a local maximum in the IV curve. As voltage further increases, the tunneling current decreases due to the misalignment of the band edges across the p-n junction. This process corresponds to the unique negative differential resistance region where the current decreases with increasing voltage. When the applied voltage increases to a specific value, the electrons gain enough energy to cross the p-n junction from the n-region conduction band to the p-region conduction band. Beyond this point, the tunnel diode begins to operate as a standard diode whose current increases with voltage.

The tunnel diode oscillator can generate a steady oscillation when the tunnel diode operates in the negative differential resistance region. This can be understood intuitively: the effective negative resistance compensates for the resistance in the circuit and thus enables a steady oscillation without dissipation. However, the steady oscillation is not only due to the effective negative resistance of the tunnel diode but also relies on the delicate features of its IV curve. The complete derivation is out of the scope of this thesis, and the step-by-step derivation can be found in reference [45].

A tunnel diode oscillator is a powerful tool for measuring physical quantities at low temperatures. It has been applied to measure magnetic susceptibility [46, 47] and quantum oscillations [48, 49].

In addition, it provides a useful probe for superconductivity as it is suitable for upper critical field [50] and London penetration depth measurements [51, 52]. These broad applications are possible because of the following advantages:

1. High precision: The precision of an tunnel diode oscillator is exceptionally high. A well-constructed tunnel diode oscillator can detect changes in oscillation frequency with a precision of 0.001 ppm [44]. Hence, it can be applied to detect tiny changes in physical quantities.

2. Little perturbation: One can conduct measurements utilizing this tool without introducing noticeable disruption. The typical frequency of the oscillator is in the tens of MHz range, corresponding to 10^{-7} eV. It is usually much smaller than the energy gap in samples of interest. The superconducting gap is on the order of 10^{-4} eV for instance. The magnetic field generated by the coil is typically in the order of mOe, which is generally not high enough to change the sample properties. For example, this field is generally smaller than the lower critical fields of most of the superconductors at temperatures not around T_c.

3. Low power: The Joule heating generated by the tunnel diode circuit is typically 1-10 mW, less than in many other measuring techniques. This low power property enables tunnel diode oscillators to be used for low-temperature measurements at 2-10 K without heating the system. Furthermore, this technique can be applied to ultra-low-temperature measurements at the milli-Kelvin range with unique designs, which will be discussed in Sec. 2.6.

4. High flexibility: Tunnel diode oscillators are small and compact, so they can be installed into various low-temperature systems. Also, this technique is compatible with other measurements, such as transport measurements, as it is a wireless/contactless measurement.

2.2 The Working Principle of Tunnel Diode Oscillators

The tunnel diode oscillator is a circuit of an LC oscillator driven by a tunnel diode. The values of LC components determine the resonant frequency. Either the inductor or capacitor of the circuit can be combined with sample of interest for measurements. Here, I introduce a homemade single layer coil as the inductor of the oscillator. To measure the magnetic properties of the sample of interest, I put the sample inside the coil. In this configuration, the effective inductance of the coil varies with the change in magnetic susceptibility of the sample inside it, as I will prove later in this section. By monitoring the oscillator's frequency, which depends on the effective inductance of the coil, one can probe the changes in the magnetic susceptibility of the sample. The relation between the frequency shift δf and the change of inductance δL is shown in the following equation,

$$f_0 + \delta f = \frac{1}{2\pi\sqrt{(L+\delta L)C}} \tag{2.1}$$

Here, I define L as the inductance of the empty coil and δL as the change of inductance due to the sample. The δL caused by the sample is generally on the order of 10 nH, which is much smaller than L that is about $1\mu H$ in our case. Then, the equation can be approximated as

$$\frac{\delta f}{f_0} \simeq -\frac{1}{2}\frac{\delta L}{L}, \tag{2.2}$$

Inductance is equal to the ratio of magnetic flux and current through the coil, so

$$\frac{\delta L}{L} = \frac{\delta \Phi}{\Phi}, \tag{2.3}$$

For a long solenoid coil, $\Phi = NH_{ac}A = nH_{ac}V_c$, where N is the number of turns of the coil, H_{ac} is the ac magnetic field generated by the coil, A is the cross-sectional area of the coil, n is the number of turns per unit length, and V_c is the volume of the coil. $\delta\Phi = nMV_s$, where M is the sample's magnetization, and V_s is the sample's volume. Hence,

$$\frac{\delta\Phi}{\Phi} = \frac{M}{H_{ac}}\frac{V_s}{V_c} = \chi_{ac}\frac{V_s}{V_c}, \tag{2.4}$$

As a result, the frequency shift can be related to the dynamic magnetic susceptibility, $\chi_{ac} = \frac{M}{H_{ac}}$.

$$\frac{\delta f}{f_0} = -\frac{1}{2}\frac{V_s}{V_c}\chi_{ac} \tag{2.5}$$

In this technique, the in-phase signal is measured, so the measured χ_{ac} is the real part of the magnetic susceptibility.

Our electrical circuit of the tunnel diode oscillator is shown in Fig. 2.2. The dc power is sent to the circuit through the same coaxial cable carrying the output signal to the equipment. The first resistor (R_1) passes the direct current into the circuit while isolating the high-frequency noise outside. The second resistor (R_2) is chosen to provide the proper bias voltage for the tunnel diode. The coupling capacitor (C_c) allows a small portion of the signal to pass through the coaxial cable for measurements. The bypass capacitor (C_b) should be large enough to work as a short path for the primary oscillation. The parasitic suppression resistor (R_p) prevents the parasitic oscillation formed by the coil and the stray capacity of the diode.

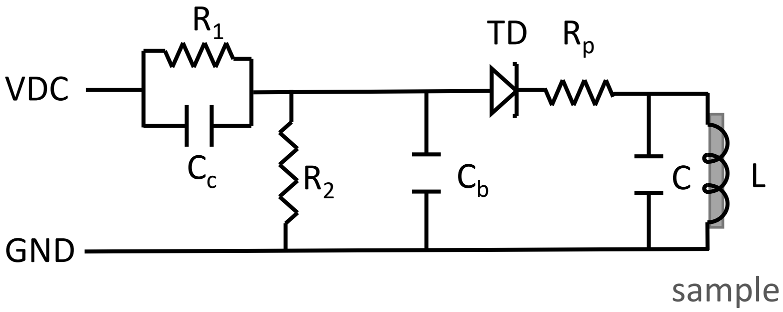

Figure 2.2: A schematic diagram of a typical electric circuit of a tunnel diode oscillator. A sample inserted in the coil is illustrated as a rectangle.

2.3 The Experimental Setup of Tunnel Diode Oscillators

The electrical components of a tunnel diode circuit may vary. Here, I discuss the typical components used in our circuits. The main component in this circuit is the germanium tunnel diode IN-3712. Its peak point current (I_p) is 1 mA, and the measured temperature-dependent IV curves are plotted in Fig. 2.3. According to the measurements, the IV curve varies with temperatures when the temperature is above 10 K but remains unchanged at low temperatures. This temperature independence at low temperatures is a general property of tunnel diodes, making TDO a suitable tool for low-temperature measurements.

The following table lists the values of the electric components we used. The TDO coils are made by a winding machine with AWS 38 copper wires. The shape and dimension of the coils are designed to match the sample size and the desired inductance. Our samples usually have slab shapes with 1-5 mm long sides. The coils are cylindrical, with a typical diameter and height

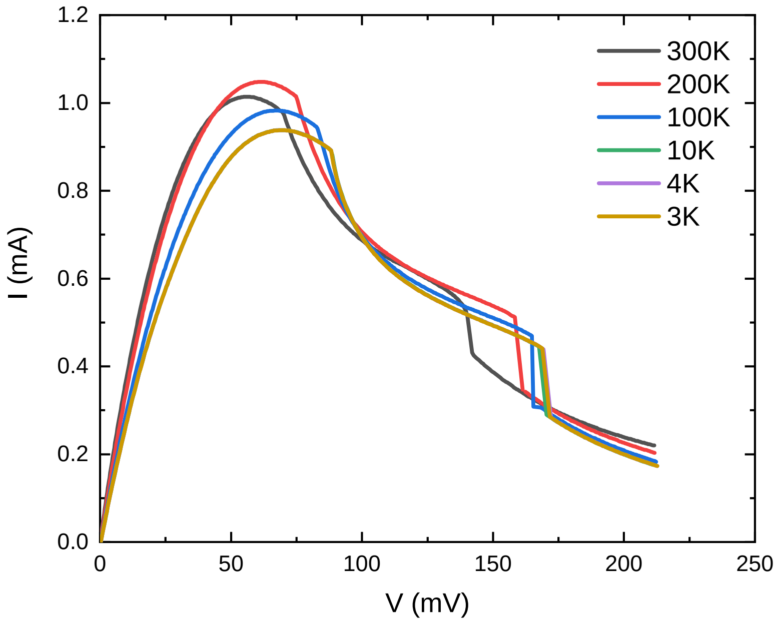

Figure 2.3: The IV characteristic curves of the IN-3712 tunnel diode at different temperatures (3 K-300 K). For temperatures under 10 K, all the curves overlap each other, indicating the diode's IV properties are stable under temperature variations at low temperature.

of 3-10 mm. The inductance value is between 0.3-1 μH, which, when combined with a 100 pF capacitor, resulted in a resonance frequency of 10-30 MHz.

Table 2.1: Typical values of components in our tunnel diode circuit.

Components	Values
I_p	$1mA$
R_1	10Ω
R_2	10Ω
R_p	10Ω
C_c	$30pF$
C_b	$270nF$
C	$100pF$
L	$0.3 - 1\mu H$

A schematic diagram of our TDO setup is illustrated in Fig. 2.4. The circuit was powered by a DC power supply (Keysight E3631A) through a coaxial cable. The resulting oscillating signal generated by the circuit was picked up through the same cable. Then, I amplified the signal 1000 times and mixed it with a standard sine wave generated by a local oscillator (AFG1062). The amplifier and mixer I used were Mini-circuits ZFL-1000-LN+ and ZFM-3-S+, respectively. The frequency of the local oscillator (f_0) was tuned to be slightly higher than the TDO frequency (f). After the mixer, the mixed signal has two components: high frequency ($f_0 + f$) and low frequency ($f_0 - f$). Passing through a band pass filter and an amplifier, the high-frequency part ($f + f_0$) was filtered out, and the remaining low-frequency part ($f_0 - f$) was amplified again. Finally, the signal was sent to a frequency counter (SR620) and an oscilloscope (MSOX3024T) for measurements. A typical signal is shown in Fig. 2.5.

Applying a mixer is not essential for TDO measurements, but it has two advantages. First, mixing can clean the signal. Two primary noise sources are the second and third harmonics generated by the circuit. Those parts will be killed after mixing since their frequencies are far

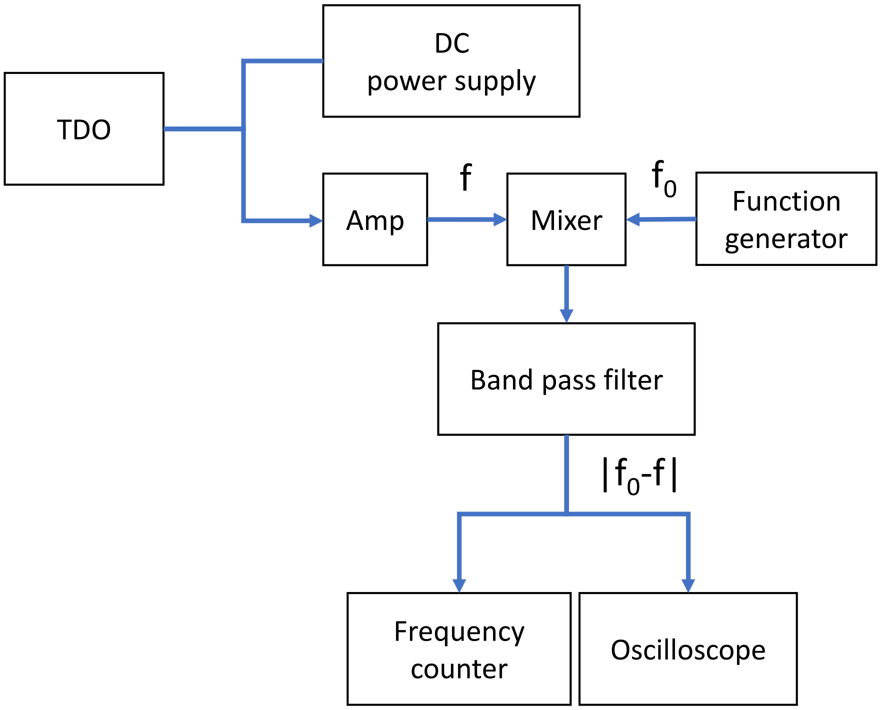

Figure 2.4: The schematic diagram of signal processing and measurements of the TDO setup. f and f_0 represent the resonant frequency of the TDO and the frequency of the local oscillator, respectively.

from the local oscillator, and a cleaner signal is thereby obtained. Second, a mixing step can increase the precision of measurements. This is because the mixed signal has a low frequency (typically 10-100 kHz), allowing more digits of the counter to record the frequency.

The resonant frequency of the tunnel diode oscillator has temperature dependency, which is mainly from the temperature dependency of the circuit components. A procedure of background subtraction is therefore introduced to reduce the temperature dependence of the circuit. A temperature-dependent measurement without any sample was taken as a background. For every measurement with the sample, the background was subtracted to eliminate the linear response of the temperature

Peaks

1	4.76837kHz	-11.0010dBV
2	5.96046kHz	-42.5537dBV
3	6.43730kHz	-52.9746dBV
4	9.53674kHz	-55.0928dBV
5	6.91414kHz	-57.1406dBV
6	0.0Hz	-57.9756dBV
7	14.0667kHz	-58.8223dBV
8	94.4138kHz	-68.2588dBV

Scale: 24.0dB/

Offset: -15.0000dBV

Bin Size: 238Hz

Sample Rate: 31.3MHz

Span 1.00MHz

Center 500kHz

Figure 2.5: A typical TDO signal that was measured on the oscilloscope. The yellow line shows the oscillations, voltage vs. time, and the white line presents its Fourier transformation. Note that this signal was measured after applying the amplifier, mixer, and band-pass filter.

dependence. However, the circuit had a nonlinear effect, so the subtracted result was still inaccurate. In Sec. 2.7, I will discuss an upgraded design, the constant-temperature TDO, in which the temperature dependency of the circuit is no longer an issue.

As mentioned in the previous section, TDO is a high-precision technique. The state of art noise level is 0.1 Hz for 100 MHz resonant frequency. However, the TDO described above has a noise problem. As shown in Fig. 2.6 a, the noise level of our circuit is on the order of 10 Hz at low temperatures, which is 100 times larger than the current ideal standard. After optimizing circuit components, selecting the power sources, applying filters, and applying electric and magnetic shielding, I narrowed down the source of the problem to the tunnel diode. The peak current of our tunnel diode (IN-3712) is 1 mA, a hundred times that of typical tunnel diodes used in TDO research. This high current feature causes a low level of differential resistance. As a result, any noise in the bias voltage generated from the DC power source will be transferred into high noise in the current. The amplification factor is 100 times greater than with typical tunnel diodes used in TDO research. Using various DC power supplies and batteries, a noise level on the order of 10 Hz is the best that can be obtained. To visualize this issue, I plot the resonant frequency vs. the bias voltage in Fig. 2.6(b). The high voltage dependence of the resonant frequency is responsible for the high noise level. A slight change in the bias voltage causes significant changes in frequency. The plot shows that the dependence is relatively low at around 0.5 V and 0.9 V, so I set the bias voltage close to those values during measurements.

This system has a heat-noise trade-off. It is necessary to lower the input voltage for low-temperature measurements in order to reduce the Joule heat, and this lower voltage leads to increased noise. For measurements at 70 mK in a dilution refrigerator (dil-fridge), the noise level rises to 30 Hz. I believe a low current tunnel diode could significantly improve the noise level.

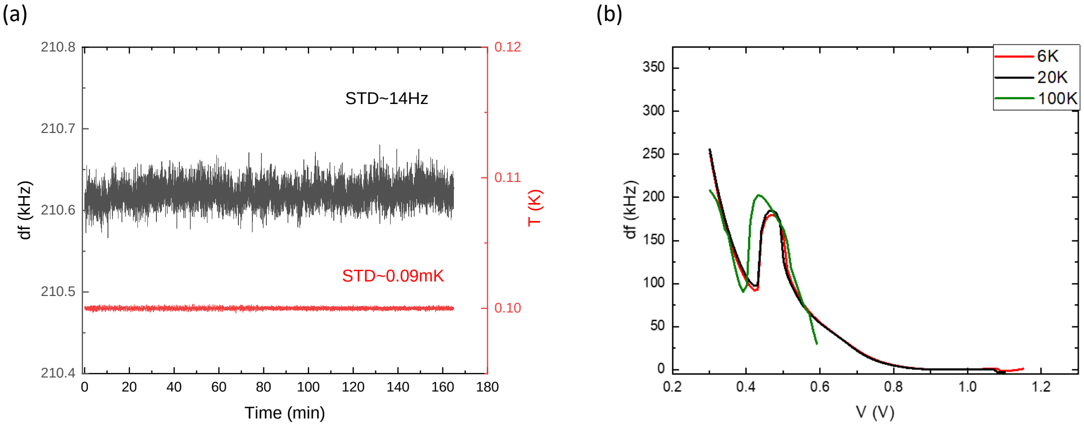

Figure 2.6: (a) A record of the TDO frequency and the dil-fridge's temperature for 160 minutes. During the measurement, the standard deviation of the frequency is 14 Hz. (b) The TDO frequency as a function of applied bias voltage on the circuit under different temperatures.

However, the supply of low-current tunnel diodes is extremely low, so I use high-current diodes for current measurements.

2.4 The TDO Device in the Physical Property Measurement System (PPMS)

To measure the magnetic susceptibility of the samples at low temperatures, I employed the Quantum Design physical property measurement system (PPMS). The operating temperature range of the PPMS is 1.8 K to 400 K with a cooling power of 10 mW at its base temperature. I designed a probe with the tunnel diode circuit to operate the tunnel diode oscillator in the PPMS. A schematic diagram of the probe is shown in Fig. 2.7. The probe is designed to be inserted into the PPMS, and its bottom part can connect to a Quantum Design universal sample puck, on which the tunnel diode circuit and coil were mounted. A homemade sample holder made of sapphire plates is used to mount the sample along desired orientations. The sample mounted on

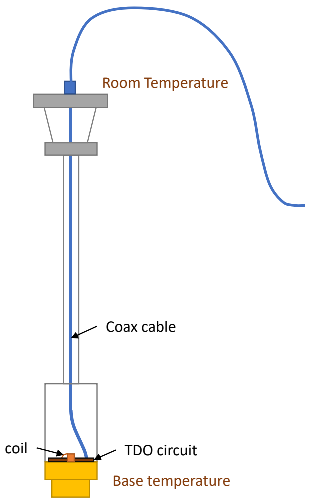

Figure 2.7: A schematic diagram of the probe used in PPMS.

the sample holder was put inside the coil. The circuit's input and output signals were passed through a homemade coaxial cable on the probe to equipment sitting at room temperature. The probe's body and the coaxial cable are made of stainless steel. This material is an excellent choice for low-temperature equipment because its thermal conductivity is only 15 W/(mK), much lower than other accessible machining materials.

2.5 The TDO Device in the Various Temperature Insert (VTI)

The compact Various Temperature Insert (VTI) is an ideal system for measurements sensitive to magnetic fields or requiring zero magnetic fields. The compact VTI is a 1K pot-based system whose base temperature is around 1.4 K. It can be inserted in various cryostats or liquid Helium storage dewars. Hence, the VTI system's environment is controllable. This advantage allows it to

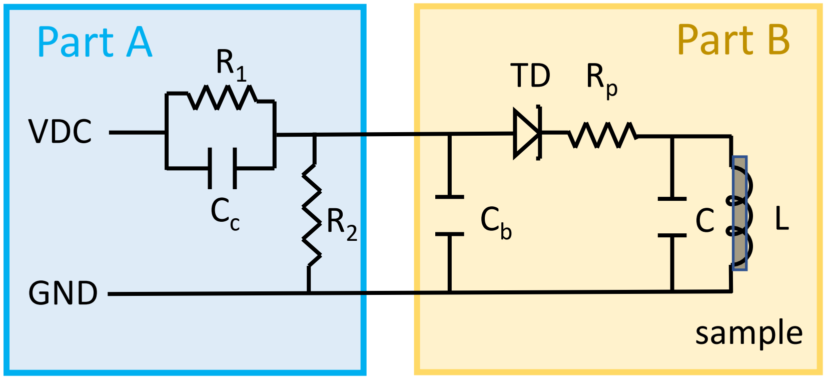

Figure 2.8: The modified TDO circuit for low temperature measurements. The circuit is separated into two parts connected by a stainless steel coaxial cable. Part B is installed on the sample stage while part A is installed on another stage for thermal dissipation.

be used for measurements requiring zero magnetic fields. For example, one of the most important applications sensitive to magnetic fields is investigating the superconductor gap symmetry by using the tunnel diode oscillator to probe London penetration depth. With a well-installed TDO, the VTI could be an ideal system for performing such experiments.

The Joule heating effect is a crucial issue for low-temperature measurements. Our TDO circuit generates 5 mW heat flux during operation, which could heat the system at low temperatures when the cooling power is insufficient. This thermal effect is more significant in the VTI system than in the PPMS because the cooling power of the VTI at its base temperature is much lower. In order to solve this heating problem, the TDO circuit was separated into two parts [53]. The circuit diagram is presented in Fig. 2.8. The first part (part A) includes the primary heat-generating components, R_1 and R_2, and the coupling capacitor. The second part includes all the critical components for measurements. I installed parts A and B on the 4K stage and the sample stage,

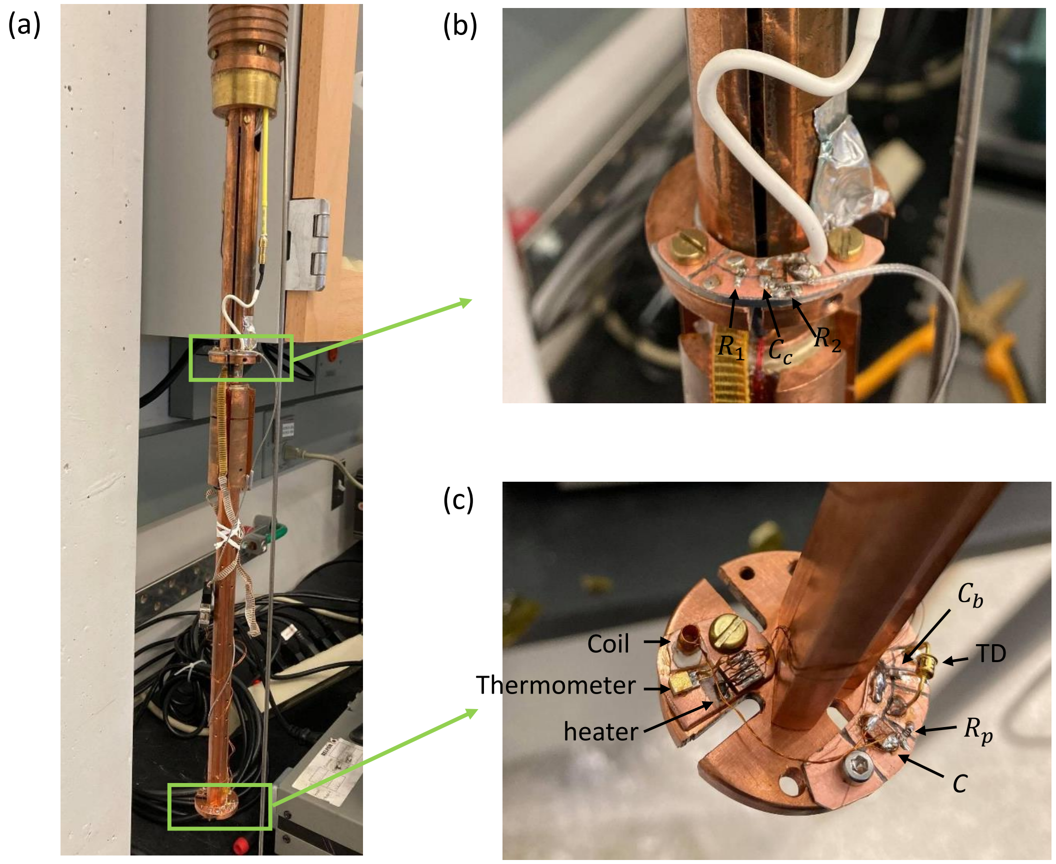

Figure 2.9: The TDO device on the VTI. Part A and part B of the circuit are mounted on the 4K stage and the bottom of the cold finger, respectively. (a) Part A of the TDO circuit. (b) Part B of the TDO circuit and the thermometer-heater pair.

respectively, and introduced a stainless-steel coaxial cable to electrically connect these two parts. Fig. 2.9 shows the TDO setup on the VTI. In this configuration, the heat generated by part A is directed into the He-4 bath through the 4K stage. As a result, the VTI system can reach its base temperature. Besides the TDO circuit, I also installed a thermometer and a heater on the sample stage to better control the sample's temperature. The thermometer is a Cernox CX-1050, and the heater is a 25 Ohm resistor. Both of them are controlled by a Lakeshore 336 temperature controller.

2.6 The TDO Device in the Dilution Refrigerator

To perform milli-Kelvin temperature measurements, I installed the TDO on the dil-fridge. The design is similar to that used in the VTI system (Sec. 2.5). I separated the TDO circuit into two parts and installed parts A and B on the still and mixing chamber stages, respectively. Most of the heat is anchored to the still stage. The base temperature of the dil-fridge is 20 mK, and the cooling power at the base temperature is 400 µW. With the operating TDO, the dil-fridge can still be cooled to 70 mK. This reflects the fact that most of the Joule heat has been efficiently dumped. I installed two TDO setups on the dil-fridge to measure two samples per cooling cycle. Fig. 2.10 shows that the two TDO circuits and coils sit directly on the mixing chamber plate. For field-dependent measurements, the TDO coils can be installed at the field center by employing additional coaxial cables. Fig. 2.11 shows an example of data taken by the TDO device in the dil-fridge. The superconducting transition was captured by the TDO clearly.

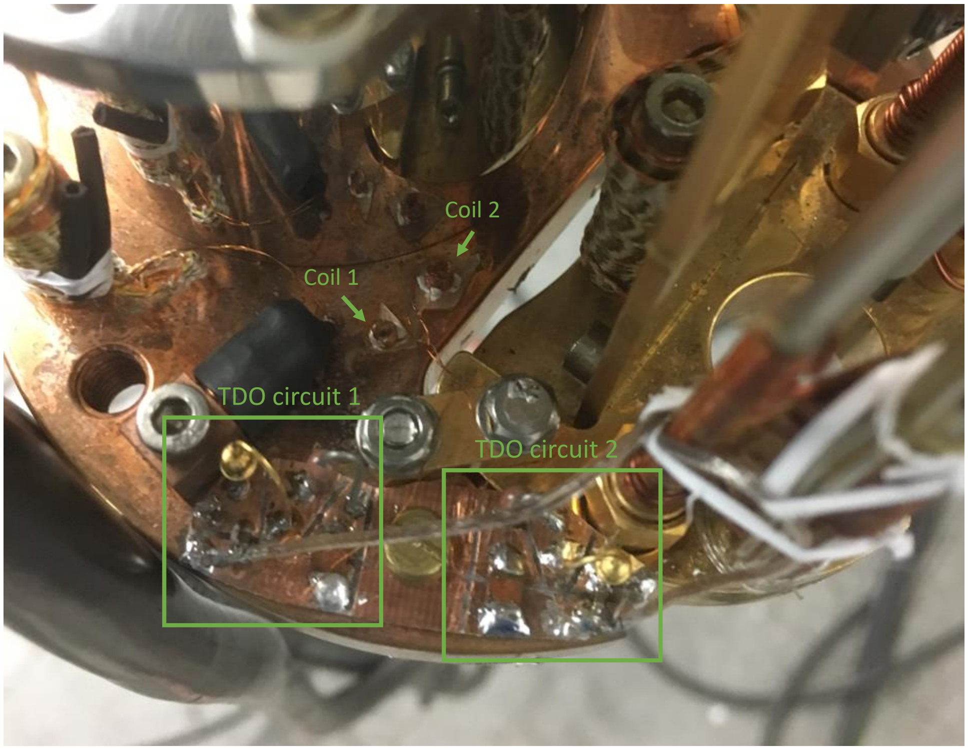

Figure 2.10: A photograph of the TDO devices mounted on the dil-fridge. The TDO circuits share one circuit board, and two TDO coils sit on the mixing chamber stage.

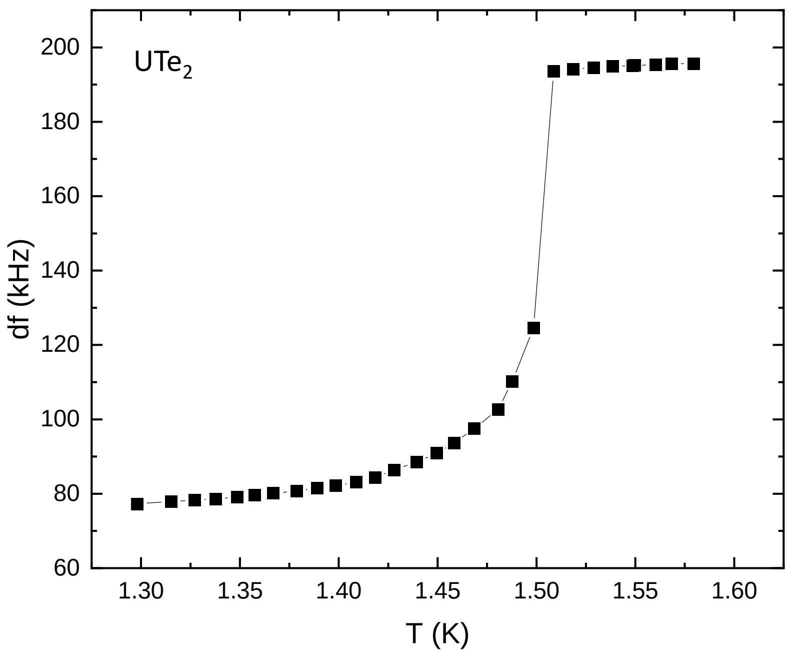

Figure 2.11: The superconducting transition of UTe$_2$ measured by our TDO device in dilution refrigerator (raw data without background subtraction).

2.7 Constant-Temperature TDO

The resonant frequency of the TDO is temperature-dependent because the electrical properties of the circuit components vary with temperature. This characteristic deforms the measuring results of temperature-dependent measurements, for example, the magnetic susceptibility vs. temperature $\chi(T)$. Most of the deformations can be removed by applying a background subtraction (Sec. 2.4), but some of the deformations remain due to the nonlinear response of the circuit. This deformation could be a severe problem for some measurements. For instance, one of the important applications of the TDO technique is to investigate superconducting pairing symmetry by measuring the penetration depth of superconductors. To acquire the pairing symmetry, high accuracy of temperature-dependence of the measuring results is required.

To eliminate the temperature deformation, I have developed a constant temperature TDO device. In this device, the sample and circuit are thermally decoupled. Using it, the circuit can be kept at a constant temperature while sweeping the sample's temperature during the measurements. Specifically, I can set the cryostat to a constant temperature and adjust the sample temperature through an additional heater-thermometer pair.

Photos and schematic diagrams of the device can be found in Fig. 2.12 and Fig. 2.13, respectively. This device is composed of a central rod, an inner tube, and an outer tube. A sectional view of the central rod is in Fig. 2.13(b). The middle part of the central rod is a copper block. This copper block is designed for sample mounting and temperature control. Its temperature determines the temperature of the sample, which is controlled by a thermometer-heater pair. I used a Cernox CX-1030 and a 100 Ohm resister as the thermometer and heater, respectively. Both of them were glued on the block through the GE varnish. In addition, they

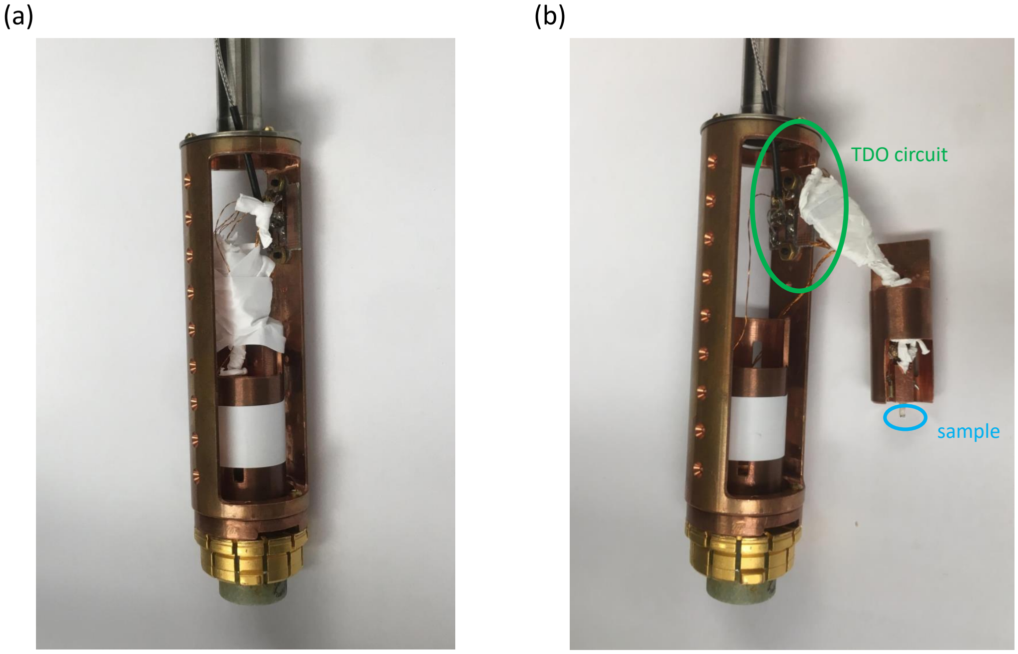

Figure 2.12: The photos of the constant-temperature TDO device on a PPMS puck. (a) The installed setup. (b) The partially installed setup with the inner tube not inseted.

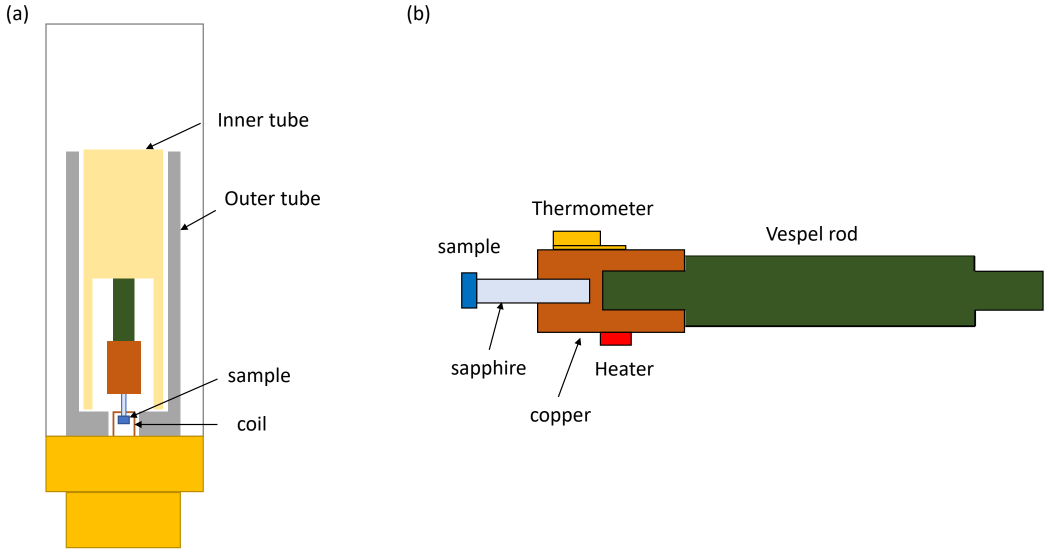

Figure 2.13: (a) A schematic diagram showing a sectional view of our constant-temperature TDO device on top of a PPMS puck. (b) A schematic diagram showing a sectional view of the central rod.

were electrically connected to the PPMS puck through manganin wires (11 Ohm for each wire). The manganin wires were introduced to ensure good thermal isolation. Through the electric cable of PPMS, the thermometer-heater pair is connected to a lakeshore 336 temperature controller.

The copper block had top and bottom holes for connections. A vespel rod and a sapphire rod were inserted into the top and bottom holes, respectively. The sapphire rod worked as a sample mount, glued to the copper block with silver epoxy. The sample was attached to the bottom of the sapphire rod with a small amount of N-grease. On the other side, a vespel rod was inserted into the top hole of the copper block as a connection to the rest of the device. The rod was glued to the top hole of the block with STYCAST. Vespel is a high-performance polyimide-based thermoplastic material characterized by low thermal conductivity. Its thermal conductivity is only 0.01 W/mK at 3K. For the rod used, the dimensions of which are 0.38” in length and 1/8” in diameter, the heat flow is less than 100 μW under a 10 K temperature difference between the two ends. Hence, it was ideal for thermally isolating the sample block from the rest of the device.

The inner and outer tubes guide the sample into the TDO coil mounted on the bottom of the outer tube. Specifically, I first glued the center rod into the inner tube then slide the inner tube into the outer tube. As a result, the sample was aligned to the center of the coil. This alignment was critical because the sample’s temperature could have been affected if there were any contact between the sample and the coil. The 3D diagram is presented in Fig. 2.14. The slots on the inner and outer tubes were designed to prevent eddy currents.

The design is compatible with various cryostats. Here, I installed the device on the PPMS probe for conducting measurements in the PPMS. The photo of the installed device is shown in Fig. 2.12. To operate it, the PPMS must be set to the high vacuum mode to avoid thermal coupling from the surrounding gas. In fact, an appropriate thermal coupling is necessary for

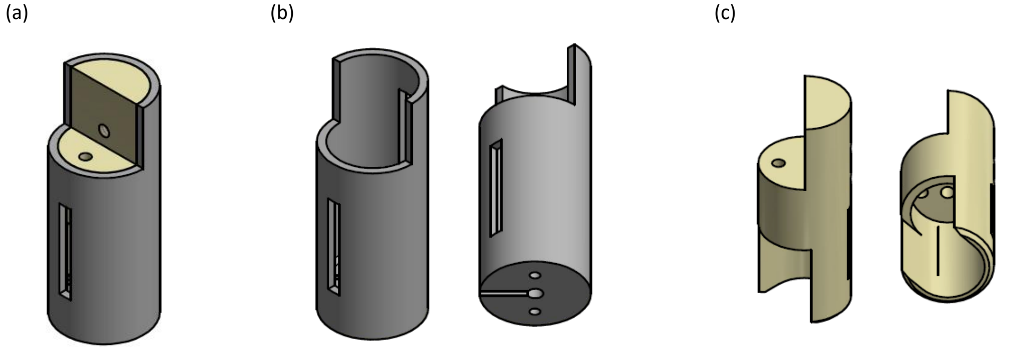

Figure 2.14: The 3D mechanical drawing of the inner and outer tubes of our constant-temperature TDO setup. (a) The combined tubes. (b) The outer tube. (c) The inner tube.

the experiment. Thermal coupling is always required for cooling the sample. If the thermal coupling is too weak, the sample might not be able to reach low enough temperatures. If the thermal coupling is too strong, it could be hard to sweep up the sample's temperature. Hence, the strength of the thermal coupling needs to be adjusted to a suitable value depending on the desired temperature range. In this device, the strength of the thermal coupling can be tuned by introducing thick copper wires between the sample block and the outer tube for different measurements.

2.8 Conclusion

In conclusion, this chapter has thoroughly detailed the development process of TDO devices specifically designed for low-temperature magnetic susceptibility measurements. The discourse covered the conception and development of four distinct devices, inclusive of three uniquely designed for various refrigerators, as well as a constant-temperature TDO device tailored for precise temperature-dependent measurements.

Our TDO's noise level is on the magnitude of about 10 Hz, with the majority of this noise emanating from a noise amplification effect attributed to high-current diodes. This noise level is sufficiently low to allow for the detection of phase transitions.

However, to broaden the range of possible applications, such as the measurement of the penetration depth of superconductors, a further reduction of the noise level is warranted. We believe that significant progress can be made in this direction by incorporating a low-current tunnel diode into our circuit, which we anticipate will yield a much lower noise level.

Chapter 3: Phase Diagram Studies of Spin Triplet Superconductor UTe_2 Under Pressures

This chapter is primarily based on the publication of W.-C. Lin et al. [24]. The sample for this study was grown by Dr. Sheng Ran at the University of Maryland. The sample was characterized by Dr. Sheng Ran and Dr. I-Lin Liu at the University of Maryland. The experimental measurements were performed by Dr. Danial Campbell and myself at the DC Field Facility of the National High Magnetic Field Laboratory (NHMFL) in Tallahassee, Florida, with the assistance of Dr. David Graf, who is a research faculty at NHMFL. The theoretical analysis was done by Dr. Andriy Nevidomskyy at Rice University.

3.1 Introduction

Previous work on uranium-based compounds such as UGe_2, URhGe and UCoGe has unearthed a rich interplay between superconductivity and ferromagnetism in this family of materials [12], with suggestions that ferromagnetic spin fluctuations can act to enhance pairing [54]. The recent discovery of superconductivity in UTe_2 has drawn strong attention owing to a fascinating list of properties – including absence of magnetic order at ambient pressure [55], Kondo correlations and extremely high upper critical fields [19] – that have led to proposals of spin-triplet pairing [19, 21, 26, 30], and a chiral order parameter [31, 56].

In addition, at least two forms of re-entrant superconductivity have been observed in high magnetic fields, including one that extends the low-field superconducting phase upon precise field alignment along the crystallographic b-axis [57], and an extreme high-field phase that onsets in pulsed magnetic fields above the paramagnetic normal state at angles tilted away from the b-axis [22].

Applied pressure has also been shown to greatly increase the superconducting critical temperature T_{c} in $\mathrm{UTe_2}$ [58, 59], from 1.6 K to nearly double that value near 10 kbar, and to induce a second superconducting phase above a few kbar [59]. Upon further pressure increase, evidence of a suppression of the Kondo energy scale leads to an abrupt disappearance of superconductivity and a transition to a magnetic ordered phase [58]. Together with the ambient pressure magnetic field-induced phenomena [22, 57, 60, 61], the axes of magnetic field, temperature and pressure provide for a very rich and interesting phase space in this system. One of the key questions is in regard to the field-polarized (FP) phase that appears to truncate superconductivity at 34.5 T under proper b-axis field alignment [22, 57], in particular regarding the nature of the coupling of the two phases and whether superconductivity could persist to even higher fields in the absence of the competing FP phase. The relation between the FP phase and the pressure-induced magnetic phase, which also competes with superconductivity [22], is similarly not yet fully understood.

In this work, we performed magnetoresistance (MR) and tunnel diode oscillator (TDO) measurements under both high hydrostatic pressures P and high magnetic fields H along the crystallographic b-axis to explore the (H, T, P) phase diagram. We find that the FP phase that interrupts superconductivity at ambient pressure is strengthened with increasing pressure, so as to suppress the transition field until there is no trace of superconductivity down to 0.4 K above 16 kbar. At higher pressures, we find evidence of a distinct magnetic phase bordered by the

FP phase at finite fields. Together with previous observations at ambient pressure, these results suggest a spectrum of magnetic interactions in UTe_2 and a multi-faceted ground state sensitive to several physical tuning parameters.

3.2 Method

Single crystals of UTe_2 were synthesized by the chemical vapor transport method as described previously [19]. The crystal structure of UTe_2 is orthorhombic and centrosymmetric, and the magnetic easy axis is the *a*-axis. Experimental measurements were conducted at the DC Field Facility of the National High Magnetic Field Laboratory (NHMFL) in Tallahassee, Florida, using a 41 T resistive magnet with a helium-3 cryostat. Resistance and magnetic susceptibility measurements were performed simultaneously on two individual samples from the same batch positioned in a non-magnetic piston-cylinder pressure cell. The pressure medium was Daphne 7575 oil, and pressure was calibrated at low temperatures by measuring the fluorescence wavelength of ruby, which has a known temperature and pressure dependence [62, 63]. The TDO technique uses an LC oscillator circuit biased by a tunnel diode whose resonant frequency is determined by the values of LC components, with the inductance L given by a coil that contains the sample under study; the change of its magnetic properties results in a change in resonant frequency proportional to the magnetic susceptibility of the sample. Although not quantitative, the TDO measurement is indeed sensitive to the sample's magnetic response within the superconducting state where the sample resistance is zero [64, 65, 66]. Fig. 3.1 shows the samples mounted in the pressure cell. Both the current direction for the standard four-wire resistance measurements and the probing field generated by the TDO coil are along crystallographic *a*-axis (easy axis). The

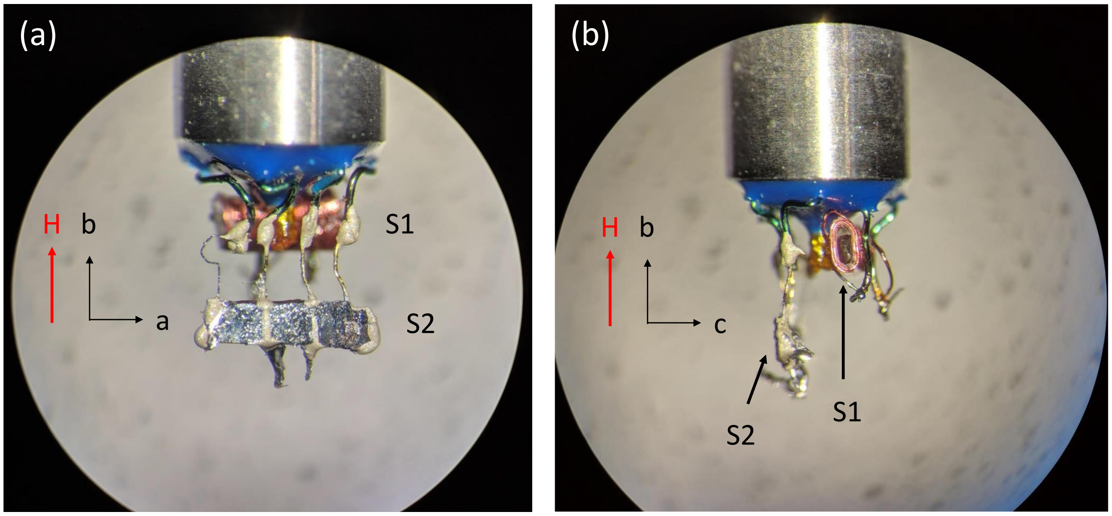

Figure 3.1: (a) The front view (b) side view of UTe_2 samples mounted in the pressure cell. The lower sample (S2) was set up for four-probe resistance measurements and the upper sample (S1) was mounted inside a coil for TDO measurements. The crystallographic axis of the two samples are aligned in the same orientation as indicated by black arrows, with applied magnetic field directed vertically along the crystallographic b-axis.

applied dc magnetic field was applied along the b-axis (hard axis) for both samples.

3.3 Phase Diagrams at Ambient Pressure

UTe_2 has fruitful phase diagrams formed by applying magnetic fields and pressures at low temperatures. Before discussing the phase evolution under pressure, we want to review the phase diagram at ambient pressure. Fig. 3.2 shows the field-angle phase diagram at 0.35 K, where the angle indicates the directions of applied fields [22]. There are multiple phases present, including a field-induced polarized phase and three superconducting phases. When the field is applied along the crystallographic b-axis, the superconducting state persists up to 35 T, bordered by a field-polarized phase. In addition, another superconducting phase presents under high magnetic

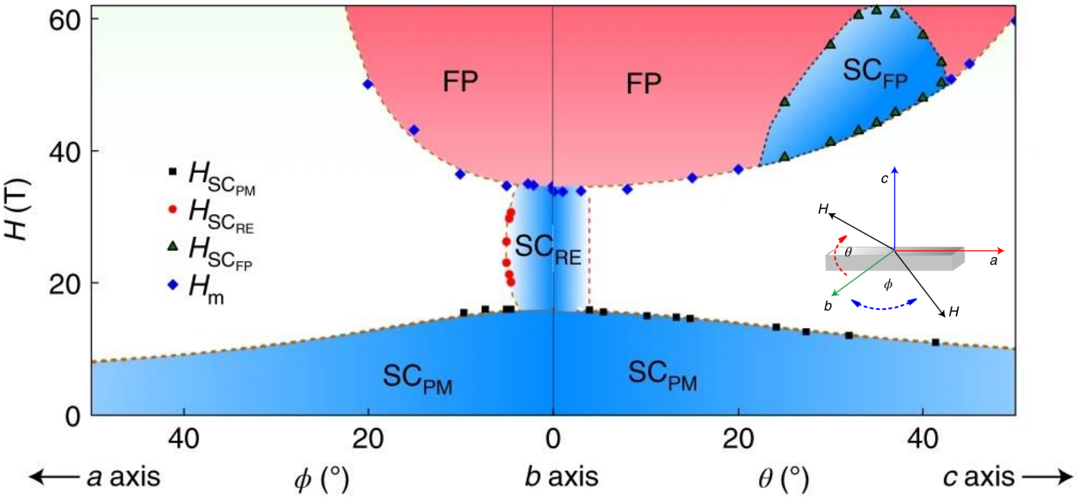

Figure 3.2: The ambient pressure phase diagram of UTe$_2$ at 0.35 K. The angles labeled on the x-axis indicates the directions of the applied magnetic fields [22].

fields applied along different directions. Its phase boundary coincides with that of the field-polarized phase. Those features indicate the interplay between the magnetic interaction and the superconductivity. Further investigations into these phases are necessary. This chapter focuses on the region where the magnetic field is along the b-axis. A pressure-dependent study for the field applied between the b- and c-axes can be found in ref. [25].

3.4 Variable Definition

I first present a representative phase diagram to illustrate the phases and variables I defined in this thesis (Fig. 3.3). In this chapter, I will discuss five phases, including a normal (N) phase, two superconducting (SC1 and SC2) phases, a field-polarized (FP) phase, and a magnetic-ordered (MO) phase (not shown here). T_c and $T_{c(2)}$ represent the superconducting critical temperature of

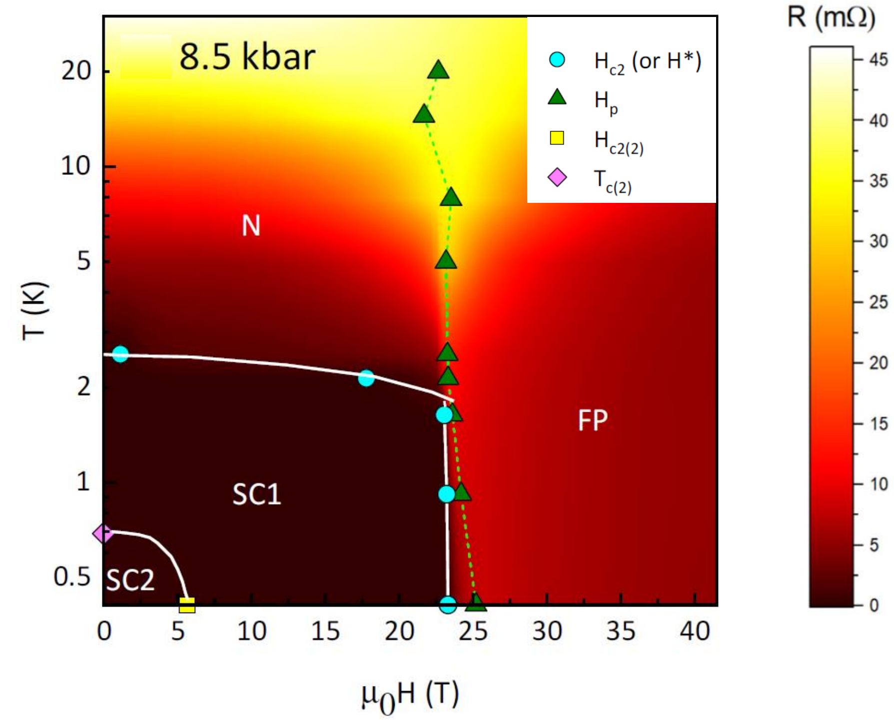

Figure 3.3: Magnetic field-temperature phase diagram of UTe_2 at 8.5 kbar for field applied along the crystallographic b-axis, with phase boundaries of superconducting (SC1 and SC2), normal (N), field-polarized (FP) phases determined by resistance and TDO data (will discuss later), and concomitant variations in resistance shown by background color contours. The cyan circles indicate the T_c transition into the SC1 superconducting phase obtained by field sweeps which are determined by zero-resistance criteria and the green triangles label the position H_p of the peak in magnetoresistance. Yellow square indicates critical field $H_{\mathrm{c}2(2)}$ of the superconducting phase SC2 based on TDO measurements (will discuss later), with pink diamonds indicating critical temperature $T_{c(2)}$ obtained from Ref. [59].

SC1 and SC2 phases, respectively. Similarly, H_{c2} and $H_{c2(2)}$ stand for the upper critical fields of SC1 and SC2 phases, respectively. The phase boundary of the SC1 phase shows a nearly vertical line at around 23 T, indicating the cutoff of superconductivity by the FP phase. This cutoff field is denoted by H^*. Lastly, H_p represents the peak in magnetoresistance.

Also, I would like to mention a few more variables in this chapter. T_M and H_{hy} correspond to the phase boundary of the MO phase, determined by the resistance measurements. P_c is defined as the critical pressure where the superconductivity demises. H_{FP} corresponds to the crossover into the FP phase when $P > P_c$, determined by the TDO measurements.

3.5 Magnetoresistance Under Pressure

The magnetic field response of electrical resistance *R* at low pressures is similar to previous results at ambient pressure, which showed that the superconducting state persists up to the FP phase transition H^* of nearly 35 T for $H \parallel b$, and re-entrant behavior can be observed near T_c for slight misalignment of the field [57]. While it is not presently known why the b-axis alignment is crucial, it is thought that alignment of applied field and fluctuating moments plays an important role [22, 57]. As shown in Fig. 3.4(a), application of 4 kbar of pressure reduces the cutoff field H^* to 30 T at 0.38 K ($T_\mathrm{c} = 1.7$ K without applied field) but retains the very sharp transition to the FP state, above which a negative MR ensues. Upon temperature increase, a re-entrant feature emerges below H^* similar to previous reports [57] but only above about 1.3 K, indicating either nearly perfect alignment along the b-axis or a reduced sensitivity to field angle at finite pressures.

Upon further pressure increase, T_c increases as previously shown [58, 59], up to 2.6 K and 2.8 K at 8.5 kbar and 14 kbar, respectively. However, H^* is continuously reduced through

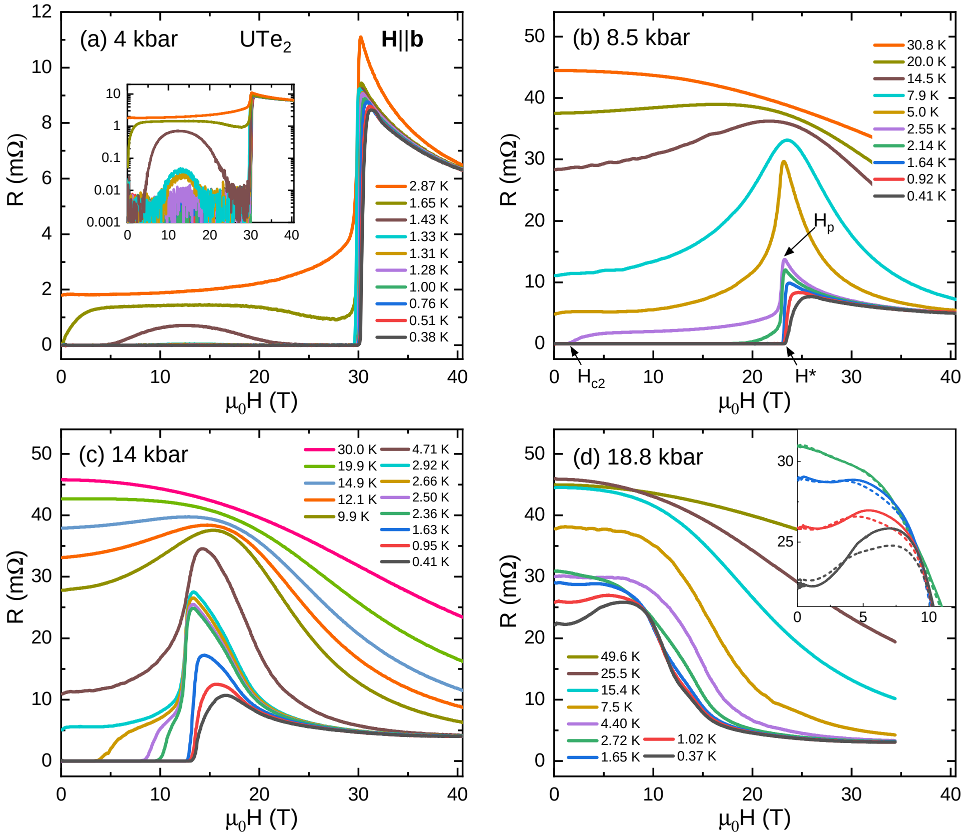

Figure 3.4: Magnetoresistance of UTe_2 under applied pressures of (a) 4 kbar, (b) 8.5 kbar, (c) 14 kbar and (d) 18.8 kbar. Inset of (a) shows a semilog plot of magnetoresistance at 4 kbar, highlighting re-entrant superconductivity. In panel (b), the applied field at the resistance peak (H_p) and the critical field (H_c2) are labelled on the violet curve as an example. The cutoff field (H^*) at base temperature is also labelled. Inset of (d) presents a zoom in the range where hysteresis is observed via distinct upsweep (solid lines) and downsweep (dashed lines) curves.

this range and changes in character. As shown in Fig. 3.4(b) and (c), at higher pressures H^* and H_{c2} dissociate, beginning as a single sudden rise with a broadened peak (denoted H_{p}) in resistance at 0.4 K that becomes better-defined upon increasing from lowest temperature, before separating into two distinct transitions at higher temperatures. Interestingly, the transition is the sharpest when the H_{c2} transition separates from H^* and moves down in field. Further, the coupled transitions slightly decrease in field until about 2 K, above which the resistive H_{c2} continues to decrease while H^* stalls (e.g. at about 12 T for 14 kbar) until washing out above approximately 20 K. This indicates a strong coupling between the two transitions that is weakened both on pressure increase and temperature increase, despite the first-order nature of the FP phase. At 18.8 kbar, shown in Fig. 3.4(d), where no superconducting phase is observed down to 0.37 K, the sharp feature associated with H^* is gone, and only a broad maximum in R remains near 8 T. Around this feature, we observed hysteresis loops at low temperature as shown in Fig. 3.5. Together with the evidence from previous pressure experiments identifying similar hysteretic behavior [58], we believe there is a magnetic ground state that evolves from zero temperature and zero magnetic field, and, similar to superconductivity at lower pressures, is truncated by the FP phase and therefore distinct from that ground state. The crossover from the magnetic ground state to the FP phase is also supported by the drop of resistance at around 10 T.

3.6 Magnetic Susceptibility Under Pressures

Figure 3.6 presents the frequency variation Δf in the TDO signal, where a minus sign has been applied to the frequency following convention. The frequency variations reflect the changes in magnetic susceptibility and therefore are sensitive to the anomalies that cannot be captured

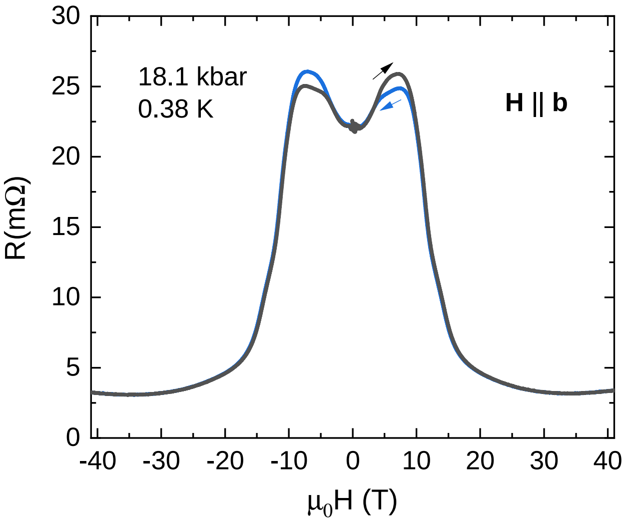

Figure 3.5: The magnetoresistance of $\mathrm{UTe_2}$ from 41 T to -41 T at 18.1 kbar. The hysteresis loops in both positive and negative field regions are consistent with the magnetic ground state.

through transport measurements in the zero-resistance regime. In addition to a sharp rise in Δf at H^*, which corresponds to a diamagnetic to paramagnetic transition, and changes in slope consistent with the re-entrant behavior shown in Fig. 3.7, there is another feature in the 4 kbar data within the superconducting state observable at lower fields. At temperatures below 1 K, Δf initially increases with field before abruptly transitioning to a constant above a characteristic field $H_{\mathrm{c2(2)}}$, and finally jumping at the H^* transition. As temperature is increased, $H_{\mathrm{c2(2)}}$ decreases in field value until it vanishes above T_{c}, tracing out an apparent phase boundary *within the superconducting state*. As shown in Fig. 3.8, the path of $H_{\mathrm{c2(2)}}$ merges with the zero-field critical temperature of the second superconducting phase "SC2" discovered by ac calorimetry measurements [59]. As shown in Fig. 3.8(a), these data identify SC2 as having a distinct $H_{\mathrm{c2}}(T)$ phase boundary from the higher-T_{c} "SC1" phase, with a zero-temperature upper critical field of approximately 11 T at 4 kbar. Upon further pressure increase, the $H_{\mathrm{c2(2)}}$ transition is suppressed in field, tracing out a reduced SC2 phase boundary (Fig. 3.8 (b)) that is absent by 14 kbar. In essence, it appears that the SC2 phase is suppressed more rapidly than the SC1 phase, which will provide insight into the distinction between each phase [32].

In contrast to the abrupt increase of Δf upon crossing H^* into the FP phase at lower pressures, the TDO signal exhibits a qualitatively different response in the high pressure regime where superconductivity is completely suppressed. As shown in Fig. 3.6(e), at 18.8 kbar Δf is almost field independent on increasing fields at 0.37 K until an abrupt drop occurs near 12 T. This drop reflects the decrease of skin depth which can be confirmed by comparing with the decrease of resistance in our transport results. However, at slightly higher fields we observe a small peak in Δf that does not match any observable feature in transport measurements. This peak suggests a metamagnetic transition at H_{FP} (= 15.5 T at 0.37 K), indicating a crossover toward the FP phase.

3.7 Phase Diagrams

Compiling this data, we summarize the observed features and phase boundaries in both resistance and TDO measurements in Fig. 3.8. We identify five phases: two superconducting phases (labeled SC1 and SC2), the normal phase (labeled N), the FP phase and the MO phase, which is only observed at 18.8 kbar. The first three phase diagrams (4, 8.5 and 14 kbar) show a smooth growth of the FP phase with pressure and the emergence of a more conventional (i.e. rounded) H-T boundary of the SC1 superconducting phase. In fact, the observable evolution of $H_{\mathrm{c2}}(T)$ at 8.5 and 14 kbar indicates a putative $H_{\mathrm{c2}}(0)$ critical point that would end within the FP phase were it not cut off by H^*. By the Werthamer–Helfand–Hohenberg (WHH) equation,

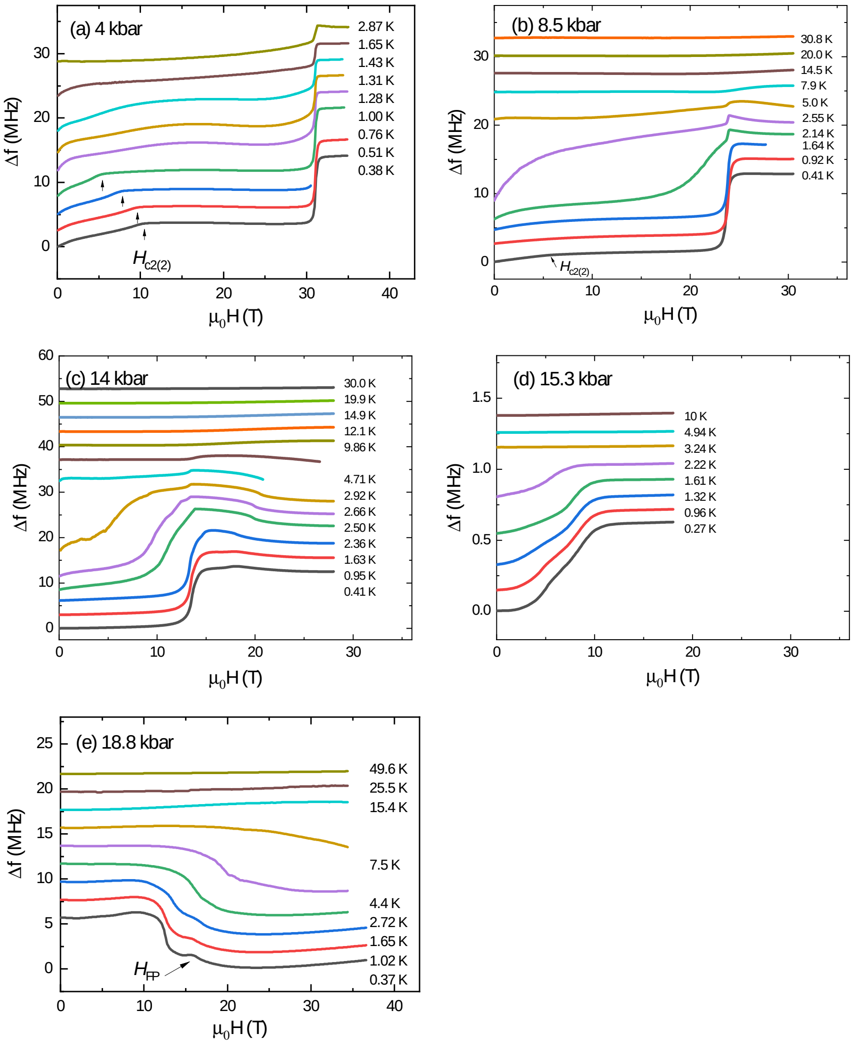

Figure 3.6: Field evolution of magnetic susceptibility of UTe$_2$ under applied pressures. The magnetic fields are applied along the crystallographic b-axis, under applied pressures of (a) 4 kbar, (b) 8.5 kbar, (c) 14 kbar, (d) 15.3 kbar and (e) 18.8 kbar. Transitions involving the SC2 superconducting phase are labelled as $H_{\mathrm{c2(2)}}$, and crossovers to the field-polarized phases (see text) labelled as H_{FP} in panel (e). All curves are vertically shifted for presentation.

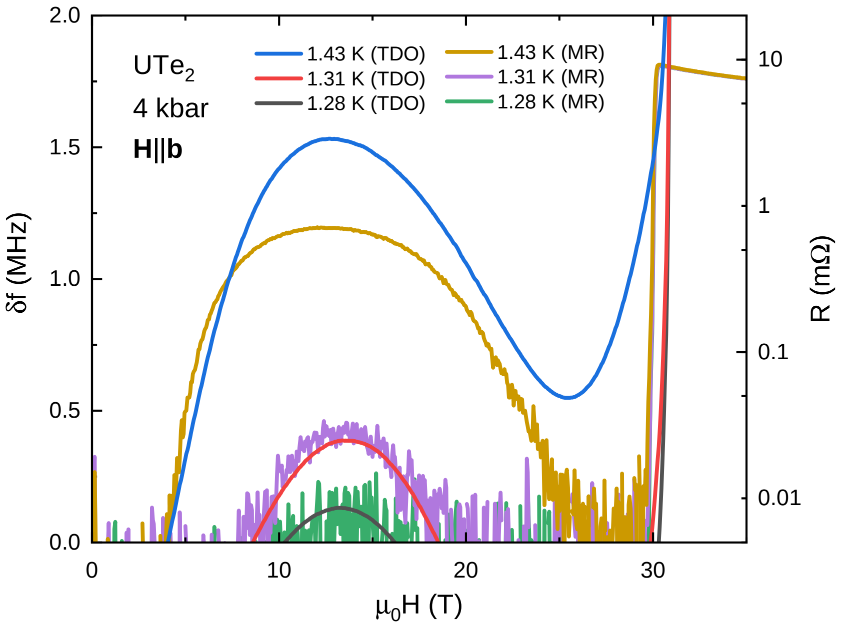

Figure 3.7: Tunnel diode oscillator (TDO) frequency variation and magnetoresistance (MR) of a single crystal UTe_2 at 4 kbar with field parallel to the b-axis, where the latter is presented in log scale. As field increases, the MR data indicates reentrant superconductivity as the resistance changes from zero to nonzero and then back to zero. Simultaneously, the sign of TDO frequency variation shows consistent results going from negative (diamagnetism) to positive (paramagnetism), and then back to negative (diamagnetism). Near 30 T, the frequency variation changes sign again as the sample enters the field-polarized phase. Note that for the TDO data, an offset as well as a small linear background (0.1MHz/T) have been applied to match the MR results.

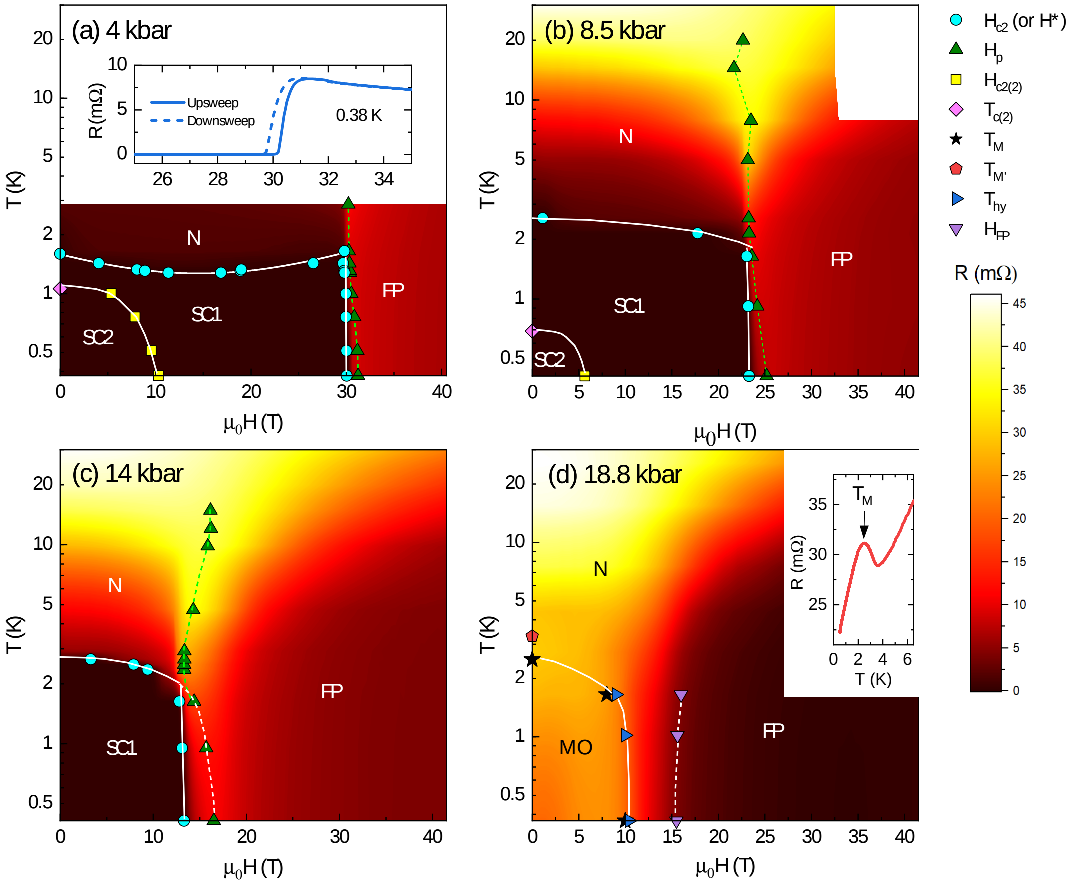

Figure 3.8: Evolution of the magnetic field-temperature phase diagram of $\mathrm{UTe_2}$ as a function of pressure for fields applied along the crystallographic b-axis, with phase boundaries of superconducting (SC1 and SC2), normal (N), field-polarized (FP) and magnetic ordered (MO) phases determined by resistance and TDO data, and concomitant variations in resistance shown by background color contours. Insert of panel (a) shows the upsweep and downsweep of magnetoresistance around the metamagnetic transition. In panels (a)-(c), the cyan circles indicate the T_c transition into the SC1 superconducting phase obtained by field sweeps which are determined by zero-resistance criteria and the green triangles label the position H_p of the peak in magnetoresistance. Yellow squares in panels (a)-(b) indicate critical field $H_{\mathrm{c}2(2)}$ of the superconducting phase SC2 based on TDO measurements (c.f. Fig. 3.6(a)), with pink diamonds indicating critical temperature $T_{c(2)}$ obtained from Ref. [59]. In panel (d), the purple downward triangles label the crossover to the field polarized state H_FP identified in TDO measurements (c.f. Fig. 4.2(b)) while the blue rightward triangles label the demise of hysteresis H_hy in transport measurements. The black star identifies the transition T_M observed in the resistance temperature dependence (panel (d) inset) while the red pentagon indicates the same transition measured in Ref. [59].

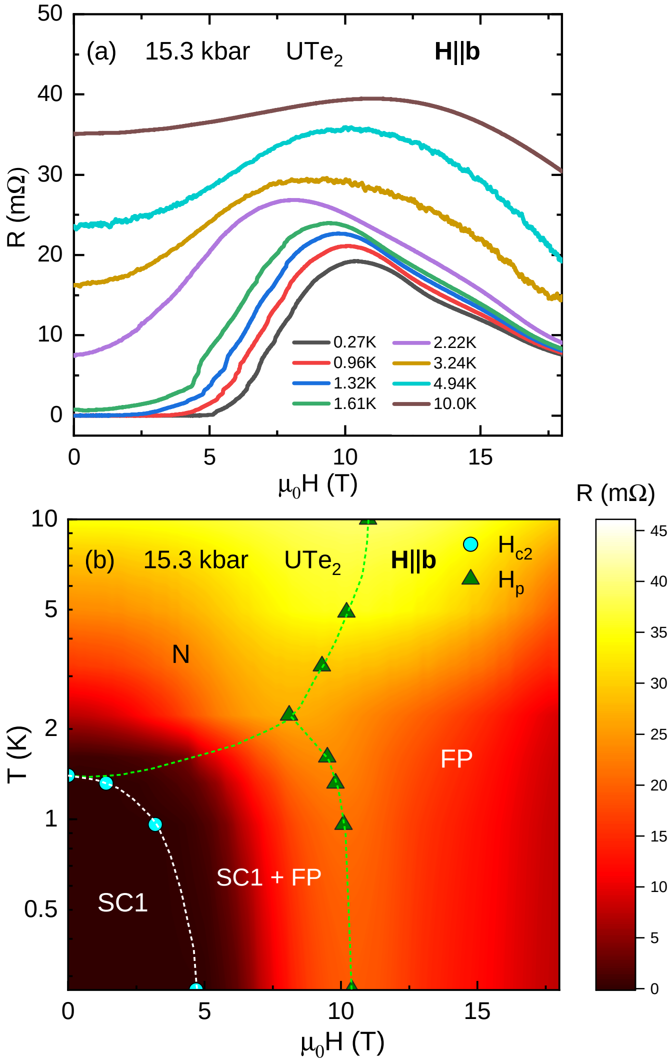

Figure 3.9: (a) Magnetoresistance and (b) field-temperature phase diagram of a UTe_2 single crystal for fields applied along the crystallographic b-axis at 15.3 kbar. The cyan circles indicate the T_c transition into the SC1 superconducting phase obtained by field sweeps which are determined by zero-resistance criteria. Green triangles label the position H_p of the peak in magnetoresistance in panels (a). Under this pressure which is close to the critical pressure P_c, the transition between the SC1 phase and FP phase broadens, resulting in a wide regime of coexistence.

we estimate these fields to be 72 T and 55 T for 8.5 kbar and 14 kbar, respectively (Fig. 3.10). In this pressure range, where the putative $H_{\mathrm{c2}}(0)$ scale becomes comparable to the FP scale H^*, there are clear indications of an influence on the shape of the FP transition as noted above, despite its first-order nature (c.f. hysteresis observed at base temperature shown in Fig. 3.8(a) inset). Tracking the resistance peak H_{p} to fields above H^* traces a non-monotonic curve that, when below T_{c}, mimics the extension of $H_{\mathrm{c2}}(T)$ of the SC1 phase, again suggesting an intimate correlation between the two phases. This is corroborated by the fact that at 18.8 kbar, when superconductivity is completely suppressed, the onset of the FP phase show a more conventional monotonic evolution with increasing field and temperature.

3.8 Theoretical Analysis on the Phase Diagram

In an effort to explain the qualitative features of the phase diagram, we consider the phenomenological GL theory describing the superconducting order parameter η. For simplicity we shall consider η to be single-component, relegating to the Appendix A the consideration of a multi-component order parameter proposed theoretically for UTe$_2$ [32, 67] and corroborated by the recent specific heat measurements [32]. The free energy consists of three parts: $F = F_{\mathrm{sc}}[\eta] + F_m[\mathbf{M}] + F_c[\eta, \mathbf{M}]$, with the first term describing the superconducting order parameter in the applied field [68]:

$$F_{\mathrm{sc}}[\eta] = \alpha(T)|\eta|^2 + \frac{\beta}{2}|\eta|^4 + K_{ij}(D_i\eta)^*(D_j\eta) + \frac{B^2}{8\pi}, \tag{3.1}$$

with $D_i = -i\nabla_i + \frac{2\pi}{\Phi_0}A_i$ denoting the covariant derivative in terms of the vector potential $\mathbf{A}$ and $\Phi_0 = h/2e$ the quantum of the magnetic flux, where $K_{ij} = \mathrm{diag}\{K_x, K_y, K_z\}$ is the effective mass tensor in the orthorhombic crystal, $K_i^{-1} = 2m_i$. The simplest way in which the

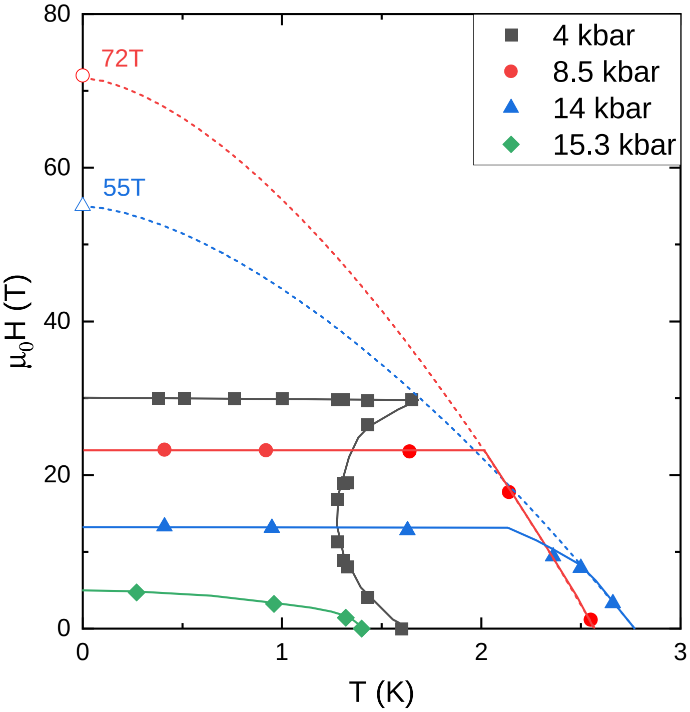

Figure 3.10: The SC1 phase boundaries of UTe_2 at different pressures with labelled putative upper critical fields. The uncommon shape of the phase boundary (i.e. flat top) suggests that the SC1 phase is truncated by the FP phase at the cutoff field H^*. The open labels indicate the putative upper critical fields which are calculated using the WHH equation 1.10. The slope of the phase boundary at T_c (i.e. $\frac{dH_{c2}}{dT}|_{T_c}$) is estimated by considering the two closest data points to T_c. The resulting upper critical fields are 72 T and 55 T for 8.5 kbar and 14 kbar. The dashed-curved lines serve as guides to the eye.

superconducting order parameter couples to the field-induced microscopic magnetization $\mathbf{M}$, is via the biquadratic interaction $F_c = g\mathbf{M}^2|\eta|^2$, where the internal magnetic field $\mathbf{B}/\mu_0 = \mathbf{M}+\mathbf{H}$. The metamagnetic transition is described by the Landau theory of magnetization with a negative quartic term ($u, v > 0$):

$$F_m[\mathbf{M}] = \frac{\mathbf{M}^2}{2\chi(P,T)} + \frac{u}{4}\mathbf{M}^4 - \frac{v}{6}\mathbf{M}^6 - \mathbf{H}\cdot\mathbf{M} \tag{3.2}$$

Taking the field $\mathbf{H}||\hat{b}$, and hence $\mathbf{A} = (Hz, 0, 0)$, we minimize the GL free energy to obtain the *linearized* gap equation of the form

$$-K_z\frac{\mathrm{d}^2\eta}{\mathrm{d}z^2} + K_x\left(\frac{2\pi H}{\Phi_0}\right)^2 z^2\eta - \alpha_0\frac{(T_\mathrm{c}-T)}{T_\mathrm{c}}\eta + g\mathbf{M}^2\eta = 0, \tag{3.3}$$

resulting in the eigenvalue spectrum similar to the problem of Landau levels for a particle in magnetic field [69]:

$$\hbar\omega_c\left(n+\frac{1}{2}\right) = \alpha_0\left(\frac{T_\mathrm{c}-T}{T_\mathrm{c}}\right) - g\mathbf{M}^2(T) \tag{3.4}$$

with the cyclotron frequency given by $\omega_c = 2eH\sqrt{K_xK_z}/\mathrm{c}$. The upper critical field $H'_{\mathrm{c2}}(T)$ is then determined from the lowest eigenvalue above:

$$H'_{\mathrm{c2}}(T) = H_0\left[\frac{T_\mathrm{c}-T}{T_\mathrm{c}} - \frac{g}{\alpha_0}M^2(H_{\mathrm{c2}})\right], \tag{3.5}$$

where $H_0 = -T_\mathrm{c}\,\frac{dH_{\mathrm{c2}}}{dT}\big|_{T_\mathrm{c}}$ is related to the slope of H_{c2} at T_c in the absence of magnetization and $\alpha_0 = \frac{\hbar^2}{2m\xi_0}$ is expressed in terms of the correlation length. The upshot of Eq. (3.5) is that the upper critical field is reduced from its bare value by the presence of the magnetization M.

The latter is a function of magnetic field, $M(H)$, to be determined from Eq. (3.2), and while its value depends on the phenomenological coefficients of the Landau theory, qualitatively the metamagnetic transition results in a sudden increase of M at H^* (by $\Delta M \approx 0.6\mu_B$ at $H^* = 34$ T at ambient pressure [57]). This then drives $H'_{\mathrm{c}2}$ down according to Eq. (3.5) and pins the upper critical field at the metamagnetic transition, explaining the sudden disappearance of superconductivity at the field H^* that marks the onset of the FP phase in Fig. 3.12. Note that the above analysis focuses on the orbital effect of the applied magnetic field, since Superconductivity in UTe$_2$ is not Pauli-limited, presumably due to the equal-spin pairing nature of the pairing [67].

It is worth discussing the value of $H_{\mathrm{c}2}$, which is of the order $H_{\mathrm{c}2} \sim 30$ T at low T and ambient pressure, much higher than would normally be inferred from $T_{\mathrm{c}} \sim 2$ K. While the analysis of the linearized GL equation above only applies in the vicinity of T_{c} and cannot, strictly speaking, be used to infer the value of $H_{\mathrm{c}2}(0)$ at zero temperature, the celebrated Werthamer–Helfand–Hohenberg theory [70] establishes a proportionality between the value of $H_{\mathrm{c}2}(0)$ and the value H_0 in Eq. (3.5). We shall therefore use

$$H_0 = \frac{\Phi_0}{2\pi\hbar^2}\frac{\alpha_0}{\sqrt{K_x K_z}} \equiv \frac{\Phi_0}{2\pi\hbar^2}\alpha_0 m^* \tag{3.6}$$

as a proxy for the upper critical field $H_{\mathrm{c}2}(0)$ ($\Phi_0 = hc/2e$ is the flux quantum). We see that the role of the effective mass is played by $m^* = (K_x K_z)^{-1/2} \propto \sqrt{m_a m_c}$ and this helps explain the high observed value of $H_{\mathrm{c}2}$ in UTe$_2$, as we show below. The key point is the quasi-two-dimensional nature of the Fermi surface sheets parallel to the c-axis, established by ARPES [71] and *ab initio* calculations [40, 67], which can be approximated by writing the dispersion as

$$\epsilon_k = \frac{\hbar^2}{2m_{ab}}\left[\left(k_a - \frac{\pi}{a}\right)^2 + \left(k_b - \frac{\pi}{b}\right)^2\right] - 2T_{\mathrm{c}}\cos(k_c d) - \mu, \tag{3.7}$$

where we have taken the in-plane mass to be isotropic for simplicity: $m_a = m_b = m_{ab}$, and T_{c} denotes the interlayer hopping strength along the c-axis (d is the unit cell height). It follows that the carrier mass along k_c can be approximated by $m_c = \hbar^2/(2T_{\mathrm{c}}d^2)$, which in turn means that the effective mass entering Eq. (3.6), $m^* \propto \sqrt{m_{ab}/(T_{\mathrm{c}}d^2)}$. Smaller magnitude of the interlayer hopping T_{c} thus results in a higher value of H_0 in Eqs. (3.5,3.6). A more rigorous treatment based on the Green's function formalism reaches qualitatively similar conclusion: $H_{\mathrm{c2}}(0) \propto 1/T_{\mathrm{c}}$ [72], thus explaining the high values of H_{c2} in UTe$_2$ due to the quasi-two-dimensional nature of the Fermi surfaces. The key finding of the present study is that H_{c2} is in fact limited from above by the metamagnetic transition at field H^*, showcased by Eq. (3.5).

3.9 Ground State Evolution

Focusing on the evolution of the ground state of UTe$_2$ with field and pressure (i.e., at our base temperature of ∼0.4 K), we present summary plots of the resistance and TDO data as well as the ground state field-pressure phase diagram in Fig. 3.12. As shown, the field boundaries of both SC1 and SC2 superconducting phases decrease monotonically with increasing pressure. However, we point out that, while the boundary of SC2 appears to be an uninterrupted upper critical field, that of SC1 is in fact the cutoff field H^*. It follows from Eq. (3.5) that this cutoff field is reduced compared to the putative H_{c2}, which would lie at higher fields if it were derived from an orbital-limited model without taking metamagnetic transition into account.

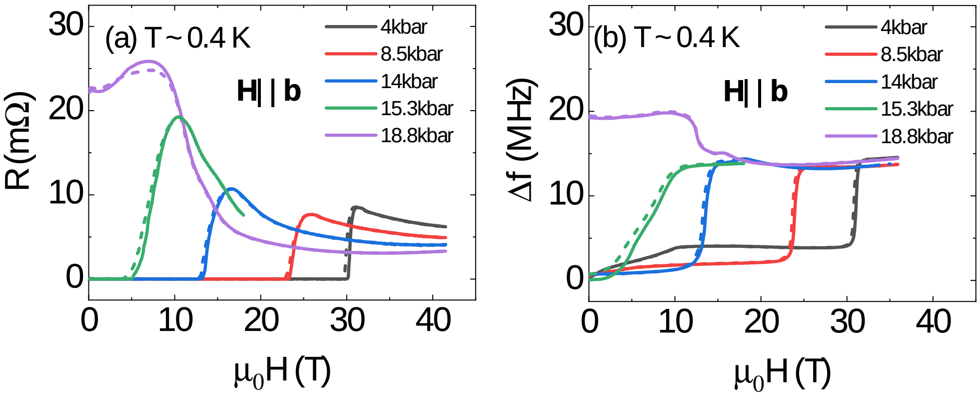

Figure 3.11: (a) Resistance and (b) TDO frequency variation as functions of applied field at fixed base temperature of the measurements. Both upsweeps (solid lines) and downsweeps (dashed lines) are plotted, indicating notable hysteresis. Note that in (b) all data are measured by a standard low-temperature-tuned TDO circuit, while the 15.3 kbar data was obtained using a room temperature-tuned circuit, and is therefore vertically scaled by a factor of 22 for comparison.

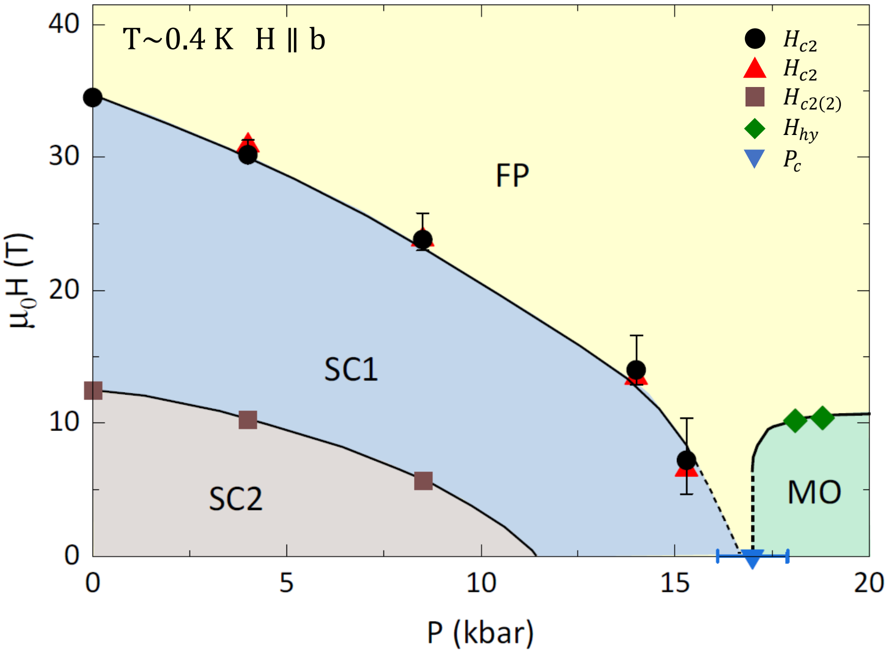

Figure 3.12: Ground state phase diagram of UTe_2 under applied field and pressure. Ground state evolution of superconducting (SC1 and SC2), field-polarized (FP) and magnetic ordered (MO) phases in UTe_2 as a function of applied pressure and magnetic field applied along the crystallographic b-axis. The phase boundary between SC1 and FP phases is determined by midpoints of resistance transitions (black circles, using average of upsweep and downsweep curves) and TDO transitions (red triangles), with error bars indicating width of transitions. Brown squares indicate the phase boundary of SC2 based on kinks in TDO frequency, and green diamonds indicate the magnetic transition determined from the resistance measurements. The blue upside down triangle labels the critical pressure (P_c) where the superconductivity demises. Zero-pressure and zero-field data points are obtained from Refs. [22] and [59], respectively. All lines are guides to the eye.

While the T_c of SC1 increases with pressure, the cutoff imposed by H^* introduces difficulty in determining whether its putative H_{c2} would also first increase with pressure. On the contrary, the unobstructed view of H_{c2} for SC2 shows a decrease with increasing pressure that is indeed consistent with the suggested decrease of the lower T_c transition observed in zero-field specific heat measurements [59].

Between 15.3 and 18.8 kbar, the H^* cutoff is completely suppressed and the MO phase onsets. While it is difficult to obtain a continuous measure of the pressure evolution through that transition, the hysteresis in transport measurements is consistent with the low-field MO phase being the true magnetic ground state of the system, separate from the FP phase. The crossover toward the FP phase under field is entirely natural from the Landau theory perspective, and the metamagnetic crossover at field H_M leads to a step-like increase in the magnetization, resulting in a small peak in TDO results.

This crossover boundary between the MO and FP phases appears much less sensitive to pressure for $P > P_c$, as evidenced by the minimal change in field value between 18.1 and 18.8 kbar. Because the experimental pressure cannot be tuned continuously, it is difficult to extract the behaviour of the crossover boundary at P_c. However, the previously observed discontinuity between the MO and SC1 phases as a function of pressure [58] suggests that the FP phase should extend down to zero field at a critical point of $P_c \sim 17$ kbar, exactly where previous zero-field work has shown an abrupt cutoff of T_c and the onset of a non-superconducting phase [59]. This is different from the case of uranium-based ferromagnetic superconductors (UGe_2, URhGe, UCoGe), where the superconductivity coexists with ferromagnetism. The distinctive behavior of UTe_2 is likely owing to a unique nature of its spin fluctuation spectrum, which may also benefit from reduced dimensions at high fields [72]. In any case, as a nearly ferromagnetic superconductor, UTe_2 provides a unique platform for future investigation of the interplay between superconductivity and magnetic phases.

3.10 Conclusion

In summary, we have explored the pressure evolution of multiple superconducting and multiple magnetic phases of UTe_2 as a function of applied pressures and magnetic fields applied along the crystallographic b-axis, where superconductivity is known to extend to the highest fields. The field-induced metamagnetic transition results in a field-polarized phase which cuts off superconductivity prematurely, as explained by a phenomenological Ginzburg–Landau theory. Under increasing pressure, the superconducting phase eventually becomes completely suppressed, at the critical pressure where we observe an onset of a distinct magnetic ordered ground state.

Chapter 4: The Unconventional Hall Effect in UTe$_2$

This chapter will discuss the unconventional Hall effect measurements of UTe$_2$ in the normal state. Most of the data were measured at the dc field facility at the National High Magnetic Field Laboratory (NHMFL) in Tallahassee, Florida, with the assistance of Dr. David Graf, who is a research faculty at NHMFL. Some of the measurements were conducted at the University of Maryland by Dr. Yun Suk Eo. The sample for this study was grown by Dr. Sheng Ran and Dr. Shanta Saha at the University of Maryland. The sample was prepared and characterized by Dr. Yun Suk Eo and me at the University of Maryland.

4.1 Introduction

The Hall effect is a fundamental phenomenon in solid-state physics that Edwin Hall discovered in 1879 [73]. It describes how a crosswise voltage is generated in relation to the flow of electric current in a material. In nonmagnetic conductors, this effect, commonly referred to as the ordinary Hall effect, necessitates a magnetic field that intersects the transport plane created by the electric current flow and the crosswise Hall voltage. The concept of the Hall effect can be simply understood by using the Drude model,

$$m\frac{d\vec{v}}{dt} = q\left(\vec{E} + \vec{v} \times \vec{B}\right) - \frac{m\vec{v}}{\tau} \tag{4.1}$$

where $\vec{v}$ is the drift velocity of the carrier, and τ is the relaxation time, describing the average time between the scattering events. By solving this equation with the current density, $\vec{J} = nq\vec{v}$, we can get

$$\begin{aligned} J_x &= \frac{\sigma}{1+(\omega_c\tau)^2}\Big(E_x + \omega_c\tau E_y\Big) \\ J_y &= \frac{\sigma}{1+(\omega_c\tau)^2}\Big(E_y + \omega_c\tau E_x\Big) \\ J_z &= \sigma E_z \end{aligned} \tag{4.2}$$

where

$$\sigma \equiv \frac{nq^2\tau}{m} \tag{4.3}$$

$$\omega_c \equiv \frac{qB_z}{m} \tag{4.4}$$

where σ is Drude's dc conductivity and ω_c is known as the cyclotron frequency describing the rotation of a charge carrier in magnetic field. When the current flows along the x direction, $J_y = J_z = 0$, we get

$$J_x = \frac{\sigma E_y}{\omega_c\tau} \tag{4.5}$$

The Hall coefficient is defined as

$$R_H \equiv \frac{E_y}{BJ_x} \tag{4.6}$$

It can be shown that

$$R_H = \frac{1}{nq} \tag{4.7}$$

The Hall coefficient or Hall resistance signifies the core electrical characteristics of the material and can be used to identify the type and concentration of charge carriers by equation 4.7.

The anomalous Hall effect (AHE), a deviation from the Hall effect not attributable to the Lorentz force, was first observed by Hall in ferromagnetic materials in 1881 [74, 75]. It typically exists in ferromagnetic conductors, transition metal oxides, diluted magnetic semiconductors, and heavy fermion systems. While AHE can spontaneously occur in ferromagnets, it requires a magnetic field intersecting the plane of voltage and current in nonmagnetic materials.

The underlying causes of the AHE can be intrinsic or extrinsic [75]. The intrinsic aspect is associated with Berry curvatures. It is called intrinsic because it does not depend on scattering centers created by disorder. The extrinsic component stems from the scattering of charge carriers by impurities through a spin-orbit coupling effect.

AHE has been detected in various heavy fermion systems, including $\mathrm{CeAl_3}$, $\mathrm{UPt_3}$, and $\mathrm{UAl_2}$ [76, 77]. In these systems, the Hall coefficient tends to surge with increasing temperature, peaking around the coherence temperature, the characteristic temperature for coherence effects, and then declines gradually. This behavior can be interpreted using skew scattering models [78]. Recently, AHE was also observed in $\mathrm{UTe_2}$ when a crosswise magnetic field was applied along the b-axis [79]. The Hall coefficient in $\mathrm{UTe_2}$ has been previously claimed to follow similar trends as other heavy fermion systems and is claimed to be consistent with skew scattering models [79].

A new type of Hall effect was recently discovered in nonmagnetic materials [80, 81], where the Hall response was generated by applying an in-plane magnetic field. This new effect is named as in-plane Hall effect (IPHE) [81]. The IPHE is a potential tool to probe topological band structures because it can be enhanced at small gap regions [82]. Another effect is the planer Hall effect (PHE), coming from the off-diagonal anisotropic magnetoresistance [83]. The IPHE can be distinguished from PHE by symmetry analysis. The Hall response in the former is an odd function in field, while the latter is an even function in field.

The origins of IPHE are discussed in recent publications [82, 84, 85, 86]. There are both intrinsic and extrinsic mechanisms. The extrinsic mechanism relates to the spin-orbit coupling and the Zeeman coupling between spin and in-plane magnetic fields. The intrinsic mechanism is associated with Berry curvature and two new band geometry quantities independent of scattering and disorder.

In this work, a series of angle-dependent Hall measurements have been done. A slab-shaped UTe_2 sample was prepared in its crystallographic ab plane. The current was along the a-axis, and the voltage drop along the b-axis was measured. Magnetic fields were applied to the UTe_2 sample mounted on a rotator up to 33 T. Surprisingly, the Hall response was strongest when the magnetic field was along the b-axis. This observation cannot be described by the ordinary Hall effect or AHE, where the out-of-plane B field is required for nonmagnetic materials. The possible origins of this phenomenon will be discussed.

4.2 The Anomalous Hall Effect in UTe_2

The AHE in UTe_2 has been recently observed by Q. NIU *et al.* [79] and I will review their results in this subsection.

The UTe_2 samples were prepared in the ac-plane with magnetic fields applied along the b-axis. In this configuration, the out-of-plane Hall effect (OPHE), where the magnetic field is out of the transport plane, was measured. According to their results, the temperature dependence follows a similar trend observed in other heavy fermion systems [76, 77]. As temperature increases, the Hall coefficient rapidly increases and starts to decline gradually when it reaches a

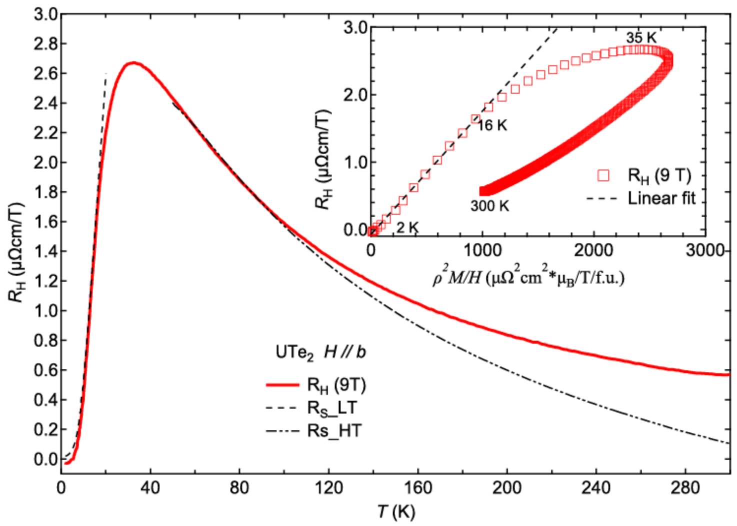

Figure 4.1: The OPHE in UTe$_2$. The sample were prepared in the ac-plane with J$\|$a and H$\|$b. The temperature dependence of the Hall coefficient between 1.4 and 300 K is shown. The different fitting curves for the AHE at low temperature ($\propto \rho^2 \frac{M}{H}$) and high temperature ($\propto \rho \frac{M}{H}$) are represented(dashed lines) [79].

peak (Fig. 4.1). It was reported in [79] that the AHE is consistent with the coherent and incoherent skew scattering models, where the coherent (incoherent) skew scattering model considers the skew scattering between the itinerant (local) f electrons and the conduction electrons. [78, 87]. Below the coherent temperature, the Hall coefficient of UTe$_2$ is suggested to be described by the coherent skew scattering model where $R_S \propto \rho_{xx}^2 \chi$. At higher temperatures, the incoherent skew scattering model is suggested, where R_S is proportional to the electrical resistivity and magnetic susceptibility ($R_S \propto \rho_{xx} \chi$). The calculated results based on these models are shown as dashed lines in Fig. 4.1. Deviations at high temperatures are thought to be caused by phonon scattering.

High field measurements reveal a metamagnetic transition at 35 T, where UTe$_2$ becomes field polarized (Fig. 4.2). A discontinuous change in the Hall coefficient occurs across this field, suggesting a Fermi-surface reconstruction [79].

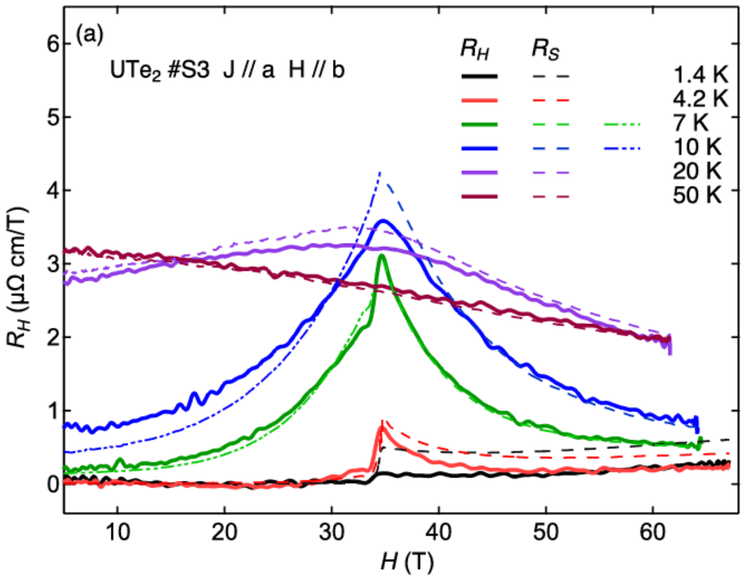

Figure 4.2: The Hall coefficient of UTe_2 with H||b up to 68 T (pulsed field). The dashed lines are estimated from the coherent (T < 20 K) and incoherent (T > 20 K) skew scattering at different temperatures. For T < 20 K, the long and short dashes correspond to the anomalous Hall signal obtained above and below the metamagnetic transition at around 35 T, respectively [79].

Figure 4.3: The prepared UTe_2 sample with three pairs of gold contacts. The two pairs along the b-axis offer two channels for the Hall measurements.

.

4.3 Method

Single crystal UTe_2 was synthesized using a vapor transport technique, as detailed in Ref. [19]. The crystal was subsequently polished into a $190\,\mu\mathrm{m}$-thick slab along its c-axis, in accordance with the natural cleavage of the crystal. The a and b-axes of the crystal were identified through magnetoresistance measurements. UTe_2 exhibits positive magnetoresistance at low temperatures when the magnetic field is parallel to the b-axis, and negative magnetoresistance when parallel to the a-axis, regardless of current direction [88]. This field-angle-dependent magnetoresistance was used to determine the crystal directions. Then, the identified crystal directions were further confirmed by magnetic susceptibility measurements.

Establishing high-quality electrical connections on the sample is critical for transport measurements. However, standard soldering methods proved to be challenging for attaching electrical contacts to the $\mathrm{UTe_2}$ surface. Thus, a thermal deposition method was employed to coat the $\mathrm{UTe_2}$ sample with chromium and gold layers. The process involved covering the transport region of the sample's surface using a photoresist, followed by etching in an acid mixture (60 mL $\mathrm{H_2O}$ + 10 mL HCl + 10 mL $\mathrm{HNO_3}$ + 10 mL $\mathrm{H_2SO_4}$) for four minutes. Subsequently, 40 Å chromium and 1200 Å gold layers were deposited onto the uncovered region, the photoresist was removed, and silver paste was applied on the gold contacts. The completed sample with gold contacts is depicted in Fig. 4.3.

The sample was then mounted on a two-axis rotator, and primary measurements were carried out at the NHMFL in Tallahassee, Florida, using a VTI within a DC field facility. Both longitudinal and transverse resistances were measured simultaneously. Two channels were used to measure the transverse resistance, and the results were found to be consistent after the anti-symmetrizing process (explained below). All data presented in this chapter is from channel 1.

Proper data processing is crucial for Hall data, as the Hall response is typically small and can be easily contaminated by the contribution of longitudinal resistance due to imperfect alignments and finite contact sizes. To eliminate the longitudinal contribution, the Hall response undergoes an anti-symmetrizing process. Given a measurement result mixed with longitudinal resistance and the Hall response, $R(H) = R_{xx}(H) + R_{xy}(H)$, the longitudinal part is an even function in field ($R_{xx}(H) = R_{xx}(-H)$), whereas the Hall response is odd in field ($R_{xy}(H) = -R_{xy}(-H)$). The longitudinal (Hall) contributions can be obtained by symmetrizing (anti-symmetrizing) for positive and negative fields as follows,

$$R_{xx}(H) = \frac{1}{2}\Big(R(H) + R(-H)\Big) \tag{4.8}$$

$$R_{xy}(H) = \frac{1}{2}\Big(R(H) - R(-H)\Big) \tag{4.9}$$

All data presented in this chapter have been symmetrized (R_{xx}) or anti-symmetrized (R_{xy}) in the field.

4.4 The Unconventional Hall Effect in UTe$_2$

Magnetic field angle-dependent Hall measurements have been performed on a UTe$_2$ single crystal. The UTe$_2$ sample was polished into a slab along its crystallographic ab-plane. The electric current was sent along the a-axis, while the Hall response was measured along the b-axis. When a magnetic field was applied along the c-axis, the OPHE was measured. Besides, the sample was mounted on a two-axis rotator. As the sample rotated, the field can be applied along various crystallographic directions. When the field was in the transport plane formed by the electric current flow and the transverse Hall voltage, an unconventional Hall effect was observed. Following the terminology used in Ref. [81], we refer to this effect as the IPHE, as the magnetic field is in the transport plane. Other possible effects will be discussed at the end of this section.

A Hall response was observed in nonmagnetic UTe$_2$ when the magnetic field was in the transport plane (Here, the ab-plane). Fig. 4.4 shows the angular dependence of longitudinal resistance (R_{xx}) and transverse resistance (R_{xy}) under 25 T when the magnetic field was rotated in the ab-plane. For T$\leq$ 40K, the R_{xx} is enhanced when the magnetic field direction is parallel to the b-axis. This enhancement relates to the metamagnetic transition at 35 T when H$||$b [22]. For higher temperatures, the R_{xx} decreases as the field rotates to b-axis, consistent with previous reports [60]. On the other hand, the R_{xy} should vanish when the field is in the transport plane for conventional nonmagnetic materials. When H$||$a, the R_{xy} of UTe$_2$ vanished as expected. As the field was rotated toward the b-axis, the R_{xy} became nonzero and reached its maximum when

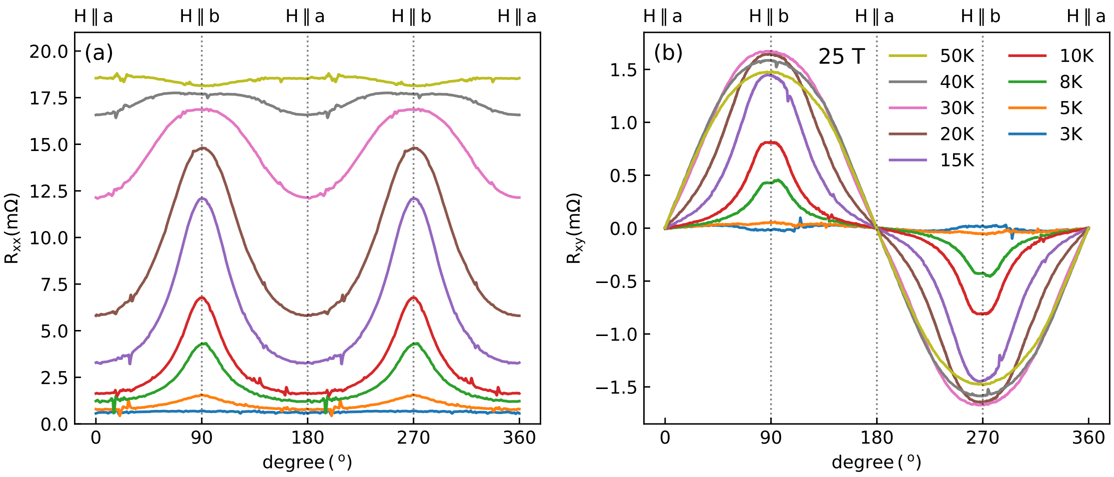

Figure 4.4: The (a) longitudinal and (b) transverse resistance of a UTe$_2$ single crystal under a 25 T magnetic field rotated in the ab-plane at different temperatures (3K-50K).

H||b.

The temperature dependence of the resistances can also be spotted in Fig. 4.4. The R_{xx} increases as temperature increases in our measuring temperature range. However, when H||b, the increment decreases as temperature increased to 50 K, implying the approach to its maximum, consistent with the result in Ref. [88]. The temperature dependence of the R_{xy} is similar. At low temperatures, the R_{xy} change sign between 3K and 5K. This behavior is consistent with the OPHE observed in the previous report [79]. It increases as temperature and reaches its maximum value at 30 K. As we will show later, this maximum value is much stronger than that of OPHE when H||c.

Similar measurements were also conducted on the bc-plane to further investigate the magnetic-field-angle dependence. The results are presented in Fig. 4.5. When H||c, the nonzero R_{xy} corresponds to the OPHE. When H||b, the R_{xy} becomes much more significant, showing a strong

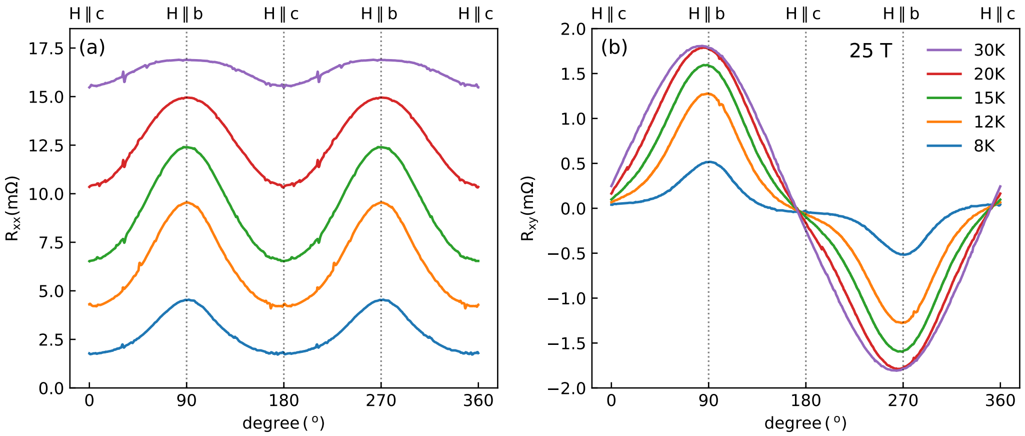

Figure 4.5: The (a) longitudinal and (b) transverse resistance of a UTe_2 single crystal under a 25 T magnetic field rotated in the bc-plane at different temperatures (8 K-30 K).

IPHE. The R_{xy} under field in the bc-plane is contributed by both the out-of-plane and the in-plane Hall response. When the field is along a certain direction, say θ degrees from the c-axis, the results are always contributed by the sum of the projections of the out-of-plane and in-plane components,

$$R_{xy} = R_{xy}^{out} cos(\theta) + R_{xy}^{in} sin(\theta) \tag{4.10}$$

Fig. 4.6 presents the decomposed result of the 30 K curve in Fig. 4.5b, showing that the in-plane component (R_{xy}^{in}) is 6.6 times that of the out-of-plane component (R_{xy}^{out}).

The field dependence of the longitudinal and the transverse resistance was measured up to 35 T, as shown in the first two panels of Fig. 4.7. Unlike typical Hall responses, the R_{xy} is nonlinear in field. At low temperatures, both the R_{xx} and R_{xy} are convex functions of field. Both R_{xx} and R_{xy} increase rapidly near 35 T, indicating a solid link to the metamagnetic transition. At 40 K, both become concave functions of field. Fig. 4.7(c) shows the relation between the R_{xx}

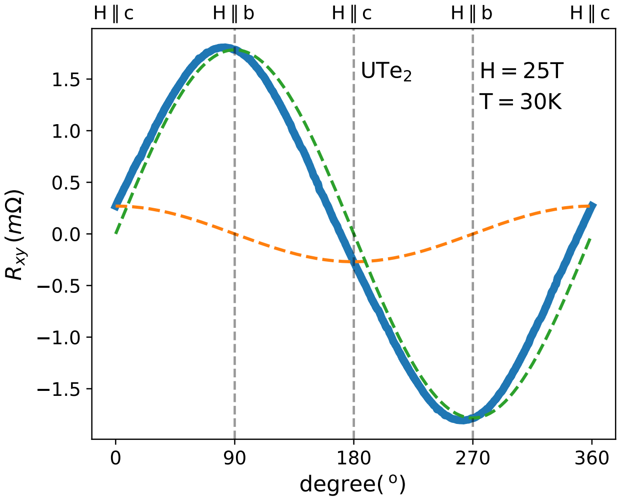

Figure 4.6: The angle dependence of the transverse resistance in UTe$_2$ for a 25 T magnetic field rotates in the bc-plane at 30 K. The result (blue curve) is decomposed into the in-plane (green-dashed line) and out-of-plane (orange dashed line) components.

and R_{xy} when H||b under positive fields up to 33 T. In the field range of 0-33 T, the R_{xy} and R_{xx} are in linear relation at low temperatures up to 10 K,

$$R_{xx}(H) = cR_{xy}(H) + R_{xx}(0) \tag{4.11}$$

where c is a constant equal to 0.12. This relation differs from that of OPHE reported in [79], where the coherent skew scattering model is used to describe the low-temperature behavior, that is $R_{xy} \propto R_{xx}^2\chi$.

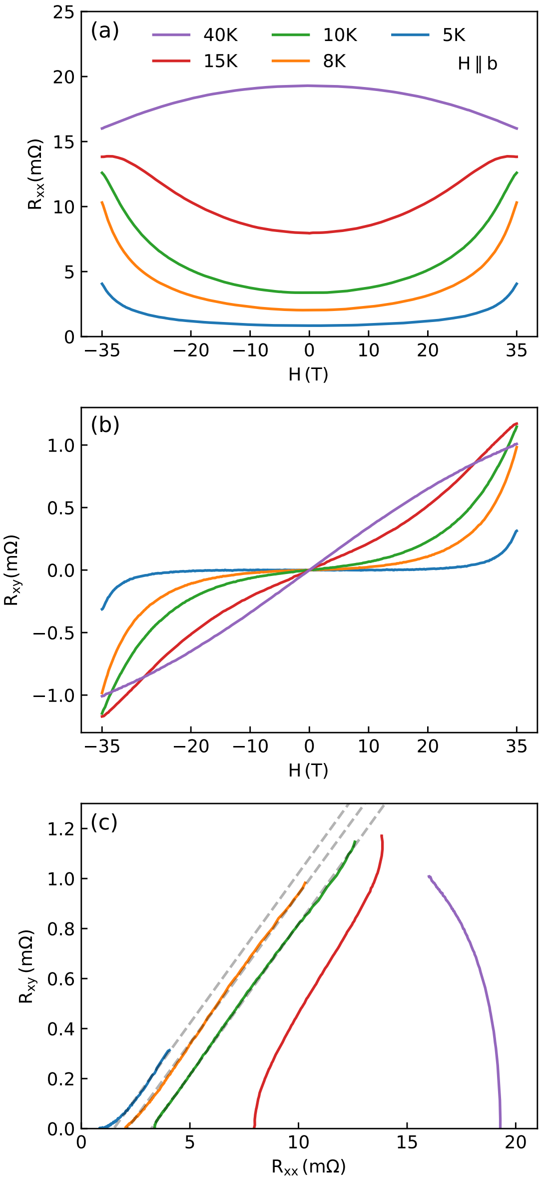

Figure 4.7: The field dependence of the (a) longitudinal and (b) transverse resistance under a magnetic field sweeping from -33 T to 33 T along the b-axis at different temperatures (5 K - 40 K). The panel (c) shows the transverse resistance as a function of the longitudinal resistance when the magnetic field sweeps from 0 T to 33 T along the b-axis.

4.5 Discussion

It's time to discuss the potential effects related to the unconventional Hall response observed in UTe_2. Our findings cannot be attributed to the ordinary or anomalous Hall effects, which require an out-of-plane magnetic field or magnetization. As a nonmagnetic material, UTe_2 cannot exhibit these effects under an in-plane magnetic field. Instead, the Planar Hall effect, which corresponds to off-diagonal anisotropic magnetoresistance, should be considered. The Planar Hall effect is characterized by even symmetry in the magnetic field, where $R_{xy}(H) = R_{xy}(-H)$. However, our measurements indicate that the R_{xy} in UTe_2 is an odd function in field, i.e., $R_{xy}(H) = -R_{xy}(-H)$, which is not consistent with the Planar Hall effect.

Another possibility is the IPHE, a newly identified phenomenon that refers to the Hall response induced by an in-plane magnetic field. Recent publications have discussed some potential intrinsic or extrinsic mechanisms behind the IPHE, but further research is needed to complete the theory [82, 84, 85, 86]. Here, we compare the known properties of IPHE with our observations.

Firstly, the Hall response of the IPHE is an odd function of field. This is consistent with our findings. Note that the presented Hall data has been undergoing the anti-symmetrizing process which, by definition, is odd in fields. Here, I want to mention that the odd parity components picked up from two channels are significant and consistent with each other. Secondly, the Onsager reciprocal relation holds in our system. In a time-reversal symmetric and Ohmic system, the Onsager relation for off-diagonal resistance is,

$$R_{ij} = R_{ji} \tag{4.12}$$

i.e., the resistance does not change by swapping the current and voltage leads. When the time-reversal symmetry is broken, the relation becomes

$$R_{ij}(B) = R_{ji}(-B) \tag{4.13}$$

where B includes all the time-reversal breaking fields. The anti-symmetrized resistance can be obtained by 4.9,

$$R^A_{ij}(B) = \frac{R_{ij}(B) - R_{ij}(-B)}{2} \tag{4.14}$$

Similarly,

$$R^A_{ji}(-B) = -\frac{R_{ji}(B) - R_{ji}(-B)}{2} \tag{4.15}$$

If the Onsager relation holds, we have

$$R^A_{ij}(B) = R^A_{ji}(-B) \tag{4.16}$$

Since the anti-symmetrized resistance is an odd function in field, $R^A_{ji}(-B) = -R^A_{ji}(B)$, the above relation is equivalent to

$$R^A_{ij}(B) = -R^A_{ji}(B) \tag{4.17}$$

Our measurements of $R^A_{ij}(B)$ and $-R^A_{ji}(B)$ are shown in Fig. 4.8. To be more clear, we write $R^A_{ij}(B)$ as $R^A_{1,2;3,4}(B)$ where 1, 2 are the number of current leads and 3, 4 are the number of voltage leads (see the inset of Fig. 4.8). Similarly, $-R^A_{ji}(B)$ is $-R^A_{3,4;1,2}(B)$ where 3,4 are the current leads and 1,2 are the voltage leads. In Fig. 4.8, the two curves match each other indicating the holding of the Onsager relation. This result is consistent with the previous report of IPHE in

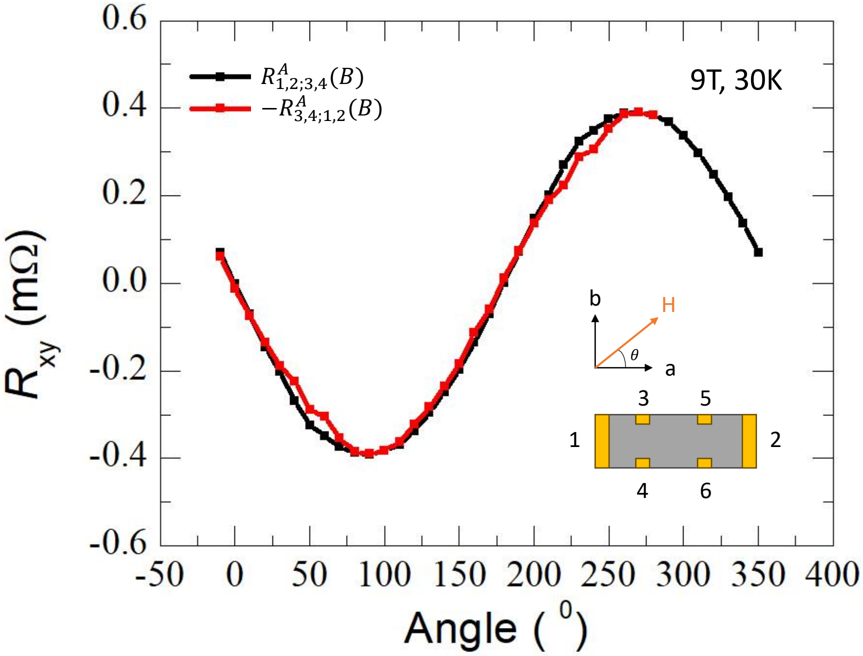

Figure 4.8: Check of the Onsager relation of R_{xy} in UTe$_2$ by comparing the anti-symmetrized Hall data with different current and voltage leads. The inset is a schematic diagram of our sample with labeled leads and crystallographic axes. The $R^{A}_{1,2;3,4}$ was measured with current leads 1, 2 and voltage leads 3, 4. The $R^{A}_{3,4;1,2}$ was measured with current leads 3, 4 and voltage leads 1, 2. The applied magnetic field is 9 T and rotates in the ab-plane at 30 K.

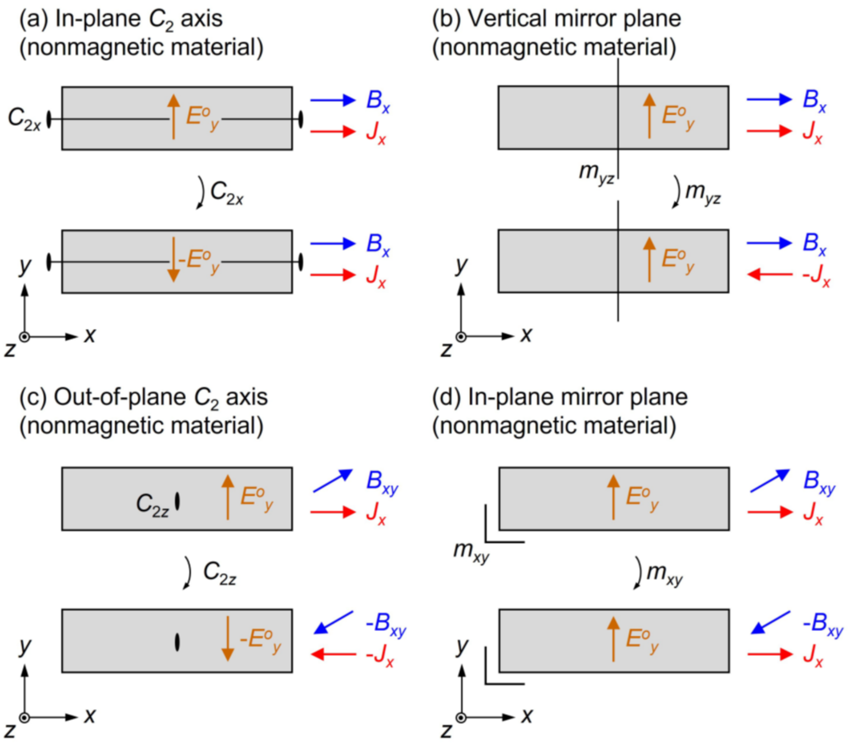

Figure 4.9: Symmetry conditions for the absence of the IPHE [89]. The superscript o indicates the odd function in field. The symmetry operations are denoted as (a) a C_2 axis along the x axis (C_{2x}, black line), (b) a vertical mirror in the yz plane (m_{yz}, black line), (c) an out-of-plane C_2 axis along the z axis (C_{2z}, black ellipse), and (d) a horizontal mirror in the xy plane (m_{xy}, black L-shape symbol).

VS-VS_2 superlattice [81].

4.6 The Symmetry Constraints on the in-plane Hall Effect

The in-plane Hall response indicates certain symmetry breaking in the system. First of all, the breaking of time-reversal symmetry is a required condition for any kind of Hall effects, including the OPHE and IPHE [90]. This condition can be fulfilled by a magnetic field or magnetization. In our system, the applied magnetic field breaks the time-reversal symmetry, releasing one of the symmetry constraints.

Besides, under certain spatial symmetries, the in-plane Hall response is forbidden [89]. Here, we list four cases for illustrative purposes (Fig. 4.9).

1. $\rho_{yx}(B_x; 0; 0)$ is zero if there is a C_2 axis along the x axis (Fig. 4.9(a)).
2. $\rho_{yx}(B_x; 0; 0)$ is zero if there is a vertical mirror symmetry m in the yz plane (Fig. 4.9(b)).
3. $\rho_{yx}(B_x; B_y; 0)$ is zero if there is a C_2 axis along the z axis (Fig. 4.9(c)).
4. $\rho_{yx}(Bx; By; 0)$ is zero if there is a horizontal mirror symmetry m in the xy plane (Fig. 4.9(d)).

Here, let us discuss the fourth case as an example. Consider a system with mirror symmetry in the xy plane (m_{xy}) and a current flowing along the x direction as illustrated in Fig. 4.9(d). By applying a reflection operation on the xy plane (m_{xy}), i.e., $x \to x, y \to y, z \to -z$, both the Hall current and the Hall electric field remain unchanged while the magnetic field along the xy plane (magnetic field lies in the transport plane when discussing the IPHE) is reversed by the xy-plane reflection.

It is worth discussing the sign change of the magnetic field under the above operation briefly. A magnetic field is a pseudo-vector resulting from taking the cross-product of two polar vectors. As a pseudo-vector, it is invariant under reflection along its direction but variant along other directions. To better understand this, consider applying the xy-plane reflection (m_{xy}) on a magnetic field along the y direction as an example. The field is driven by a cyclotron motion in the xz plane. The motion will be reversed by changing z to -z. As a result, the corresponding magnetic field generated by the reversed cyclotron motion is also reversed.

Now, we have a system after the xy-plane reflection operation, including the unchanged electric field, the unchanged current, and the reversed magnetic field. In this reflected system, the original Hall equation,

$$E_y = \rho_{xy}(H) J_x \tag{4.18}$$

becomes

$$E_y = \rho_{xy}(-H) J_x \tag{4.19}$$

Since the in-plane response is an odd function in field, i.e., $\rho_{yx}(-H) = -\rho_{yx}(H)$, the above equation is equivalent to

$$E_y = -\rho_{xy}(H) J_x \tag{4.20}$$

With m_{xy} symmetry, the equation should be invariant under xy-plane reflection, so equation 4.18 should be equivalent to equation 4.20. This results in a zero Hall resistivity. Similar arguments can be made for the other listed cases.

4.7 The Symmetry Analysis on IPHE Systems

Our observations of the in-plane Hall response in UTe_2 indicate the symmetry lowering in its parent crystal symmetries. UTe_2 has an orthorhombic crystal structure in the $Immm$ (No.71) space group with three translational symmetries, three mirror planes, and three 2-fold screw axes in a body-centered lattice. Among these symmetries, the mirror symmetries restrict the Hall conductance. Our experimental setup, shown in the top panel of Fig. 4.10, involved sending current along the a-axis while measuring the Hall response along the b-axis. According to our results, the IPHE presents when the magnetic field was parallel to the b-axis. With a simple mapping ($a \rightarrow x, b \rightarrow y, c \rightarrow z$), it is easy to show that this configuration corresponds to

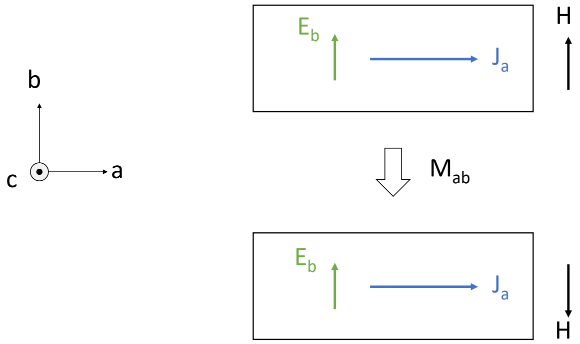

Figure 4.10: The schematic configuration of the Hall measurement in UTe_2 when H||b (top panel) and the configuration after applying the ab-plane reflection (bottom panel).

the fourth case of symmetry restrictions, where the Hall response is forbidden. Therefore, we conclude that the IPHE in UTe_2 indicates the breaking of ab-plane mirror symmetry in our system.

IPHE has been reported in other nonmagnetic systems such as the VS-VS_2 superlattice and the semimetal $ZrTe_5$. Here, I will briefly discuss the symmetry conditions of IPHE in their systems. The VS-VS_2 superlattice has the monoclinic $C2/m$ space group with a glide mirror symmetry $\widetilde{m}_{xz}$. The IPHE was observed in the xy plane under a magnetic field along the x direction. In this configuration, the Hall response was not restricted by the system's symmetry [89]. On the other hand, in $ZrTe_5$, the IPHE was forbidden by its orthorhombic $Cmcm$ crystal symmetry, which has bc-plane and ac-plane mirror symmetries. The experimental setup involved sending current along the a-axis and measuring the Hall field along the c-axis with the magnetic field along the c-axis. By mapping the a, b, c directions to x, -z, y directions, respectively, one can find that this configuration also corresponded to the fourth case of symmetry restrictions, similar to our UTe_2 system. In conclusion, the IPHE in $ZrTe_5$ is also forbidden by its crystal symmetry.

4.8 Conclusion

In wrapping up this chapter, our research has led to the discovery of an unconventional Hall effect in UTe_2. This effect is observable when the magnetic field is located within the transport plane (ab-plane). We noted the most vigorous response when the field was aligned parallel to the b-axis, while no response was detected when parallel to the a-axis. We found that this unique Hall response peaks around 30 K and reverses its sign at 3 K as the temperature descends.

At low temperatures, the Hall response exhibits a noticeable amplification when the field increases to 33 T. This behavior suggests a strong correlation with the metamagnetic transition occurring near 35 T. To validate this correlation, additional investigations under a higher field are necessary. Moreover, we have discerned a linear relationship in fields between the longitudinal resistance (R_{xx}) and the Hall response (R_{xy}) at low temperatures (T$\leq$10K), which cannot be explained by the coherent skew scattering model that is used to describe the Hall effect in heavy fermion compounds.

Guided by reference [81], we've classified this phenomenon as the IPHE, attributable to its odd symmetry in the field. The emergence of IPHE, reinforced by a symmetry analysis, leads us to conclude that one of the crystalline symmetries - the ab-plane mirror symmetry - is broken. To fully comprehend this symmetry breaking, more in-depth microscopic studies are warranted. Finally, it's important to note that the origins of IPHE within UTe_2 remain unexplored, necessitating further theoretical research.

Chapter 5: Conclusions and Outlook

In this thesis, I summarized the developing process of tunnel diode oscillators (TDO) for magnetic susceptibility measurements. Furthermore, I presented the high field studies of the unconventional superconductor UTe_2, focusing on the pressure evolution phase diagram and the unconventional Hall effect.

In Chapter 2, I delved into the development process of TDOs for magnetic susceptibility measurements. The journey encompassed the development of four distinct devices, each tailored for different refrigeration applications. Future works should focus on reducing the noise level of TDOs by incorporating low-current tunnel diodes into our circuits. This will extend their range of applications toward measuring the penetration depth of superconductors.

In Chapter 3, our focus shifted to the investigation of the pressure evolution of multiple superconducting and magnetic phases of UTe_2 under magnetic fields along the crystallographic b-axis. By utilizing the TDO, multiple superconducting phases have been identified. In addition, the confinement of superconductivity by the metamagnetic transition has been explained by a phenomenological Ginzburg-Landau theory. As increasing pressure, superconductivity completely vanished at the critical pressure where a magnetic ordering phase emerges.

Chapter 4 unfolded a distinctive discovery of an unconventional Hall effect in UTe_2. The unique Hall response, peaking around 30 K and reversing its sign at 3 K, is likely coupled with the metamagnetic transition at low temperatures. The discovery, including the nature of odd symmetry in fields, led us to categorize this phenomenon as the in-plane Hall Effect (IPHE), suggestive of a broken ab-plane mirror symmetry in our UTe_2 system. However, the origins of IPHE within UTe_2 remain a mystery, warranting further exploration and theoretical research.

In essence, this thesis has not only contributed to our understanding of TDOs and the unique properties of UTe_2 but also opened up new avenues for future research. The pursuit of reducing noise in TDOs, further exploration of the pressure-dependent superconducting and magnetic phases in UTe_2, and the untangling of the origins of IPHE represent promising future research directions. It is our hope that these findings and insights serve as a stepping stone for future endeavors in these exciting domains.

Appendix A: Details of the Ginzburg–Landau Theory

In the Sec.3.8, we have focused on a single-component superconducting order parameter for simplicity. At the same time, it has been suggested that the order parameter in $\mathrm{UTe_2}$ may be two-component and have a non-zero magnetic moment of the Cooper pair aligned along the field direction – the so-called nonunitary triplet superconductor. This section analyzes the theoretical predictions for the upper critical field in this case.

A.1 Two-component order parameter

The odd-wave superconductor, such as believed to be the case in $\mathrm{UTe_2}$, is described by an order parameter $\hat{\Delta}(\mathbf{k}) = i(\vec{d}_{\mathbf{k}} \cdot \vec{\sigma})\sigma_2$ expressed in terms of the $\vec{d}$-vector. The superconducting order parameter in a crystal can be decomposed into a linear superposition of the irreducible representations $\Gamma_i(\hat{\mathbf{k}})$ of the point-group symmetry:

$$\vec{d}(\mathbf{k}) = \sum_i \vec{\eta}_i \Gamma_i(\hat{\mathbf{k}}). \tag{A.1}$$

In the case of $\mathrm{UTe_2}$, the point group D_{2h} contains only the one-dimensional representations, which would generically have different transition temperatures. As a result, the single-component order parameter, for which the Ginzburg–Landau (GL) theory has been presented in the main text, is expected to provide a sufficient description.

However, it has been pointed out that in a strong magnetic field, along for instance the crystallographic $\hat{b}$ direction, the point group symmetry is lowered to C_{2h}, allowing for a linear superposition of the two irreducible representations, such as B_{1u} and B_{3u} [91]. Therefore, we shall consider a two-component order parameter which encodes the expression for the $\vec{d}$-vector as a linear combination of these two irreducible representations [67]:

$$\vec{d}(\mathbf{k}) = \eta_x \hat{d}_{B_{3u}}(\mathbf{k}) + \eta_y \hat{d}_{B_{1u}}(\mathbf{k}) \tag{A.2}$$

Given the field in the $\hat{b}$ direction, it is convenient to choose the coordinate system $(a, b, c) \to (y, z, x)$. In this notation, it was shown in Ref. [67] that the leading components of the B_{1u} and B_{3u} irreducible representations take the form:

$$\begin{aligned} \vec{d}_{B_{3u}}(\mathbf{k}) &\sim \sin(k_b b)\, \hat{c} \,\propto\, (1, 0, 0) && \text{(A.3)} \\ \vec{d}_{B_{1u}}(\mathbf{k}) &\sim \sin(k_b b)\, \hat{a} \,\propto\, (0, 1, 0), && \text{(A.4)} \end{aligned}$$

so that the two-component order parameter transforms like the $\boldsymbol{\eta} = (\eta_x, \eta_y)$ vector in the xy-plane. Written explicitly as a matrix in the spin space, the superconducting order parameters takes on the following form:

$$\hat{\Delta} = i(\vec{d} \cdot \sigma)\sigma_2 = \Delta_0(\mathbf{k}) \begin{pmatrix} -\eta_x + i\eta_y & 0 \\ 0 & \eta_x + i\eta_y \end{pmatrix}. \tag{A.5}$$

Notice that the absence of the z-component of the d-vector (along the applied field direction) means that the order parameter matrix is diagonal, describing *equal-spin pairing* [67].

The most general Ginzburg–Landau theory allowed by orthorhombic symmetry can be split into two contributions: $F[\boldsymbol{\eta}] = F_0[\boldsymbol{\eta}] + F_B[\boldsymbol{\eta}]$, the first term being the zero-field Landau free energy

$$F_0[\boldsymbol{\eta}] = \alpha_x|\eta_x|^2 + \alpha_y|\eta_y|^2 + \frac{\beta_1}{2}(\boldsymbol{\eta}\cdot\boldsymbol{\eta}^*)^2 + \frac{\beta_2}{2}|\boldsymbol{\eta}\cdot\boldsymbol{\eta}|^2 + \frac{\beta_x}{2}|\eta_x|^4 + \frac{\beta_y}{2}|\eta_y|^4,$$

where we have allowed for the xy anisotropy due to the orthorhombicity. In particular, $\alpha_x(T) \neq \alpha_y(T)$ allows, in principle, for different critical temperatures for the two components of $\boldsymbol{\eta}$, corroborated by two distinct signatures in the temperature dependence of the specific heat data [32].

The gradient terms [68] also contribute to the free energy, and become relevant when computing the upper critical field:

$$F_B[\boldsymbol{\eta}] = \frac{B^2}{8\pi} + K_1(D_i\eta_j)^*(D_i\eta_j) + K_2(D_i\eta_i)^*(D_j\eta_j) + K_3(D_i\eta_j)^*(D_j\eta_i) + F_{\text{ani}}[\boldsymbol{\eta}]$$

where the Einstein summation is implied over repeated indices $i, j = \{x, y\}$ and $D_i = -i\nabla_i + \frac{2\pi}{\Phi_0}A_i$ denotes the covariant derivative in the presence of the external vector potential $\mathbf{A}$. In addition to the above terms, the orthorhombic symmetry of the crystal allows to write down three more terms which we grouped into F_{ani} [68]:

$$F_{\text{ani}}[\boldsymbol{\eta}] = K_x(D_x\eta_1)^*(D_x\eta_1) + K_y(D_y\eta_2)^*(D_y\eta_2) + K_z(D_z\eta_i)^*(D_z\eta_i). \tag{A.6}$$

Note that the coefficients K_a play the role of $\hbar^2/2m_a$ in the traditional form often used to write down the GL equations, and the orthorhombic symmetry means that the effective mass tensor is anisotropic.

The applied magnetic field polarizes the electron spins in the normal state, resulting in the internal magnetization $\mathbf{M}(H)$. The free energy now contains additional terms coupling the superconducting order parameter to the magnetization:

$$F_{\text{coupl}}[\boldsymbol{\eta}, \mathbf{M}] = g\mathbf{M}^2(\boldsymbol{\eta} \cdot \boldsymbol{\eta}^*) - w(\mathbf{M} + \mathbf{H}) \cdot (i\boldsymbol{\eta} \times \boldsymbol{\eta}^*), \tag{A.7}$$

The first term is the same as in the main text, whereas the second term describes the interaction of the total magnetic field $\mathbf{B} = \mu_0(\mathbf{M} + \mathbf{H})$ with the internal moment of the Cooper pair. This last term only appears in the *nonunitary* state where $\boldsymbol{\eta}^*$ is not collinear with $\boldsymbol{\eta}$, such as for instance

$$\boldsymbol{\eta}_{\text{chiral}} = (1,\, i\delta), \tag{A.8}$$

where δ is taken to be real (generically, $|\delta| \neq 1$ because of the absence of C_4 rotation in the xy-plane). Note that we do not need to consider the pair-breaking effect of the internal Zeeman field, due to the equal-spin pairing nature of the order parameter in Eq. (A.5). Indeed, this is consistent with the experimental evidence that H_{c2} exceeds the Pauli–Clogston limit in UTe$_2$ for field $H \parallel \hat{b}$.

We consider now the field along the $\hat{z}$ (i.e. crystalographic $\hat{b}$) direction, as in the experiment, and choose the gauge where $\mathbf{A} = (-Hy, 0, 0)$. Differentiating with respect to η_j^* $(j = x, y)$ and dropping the quartic terms in the free energy, we obtain the linearized GL equation in the form of two differential equations for η_x and η_y:

$$(K_{123}+K_x)D_x^2\eta_x + K_1 D_y^2\eta_x + \tilde{\alpha}_x(T)\eta_x + (K_2 D_x D_y + K_3 D_y D_x)\eta_y - iw(M+H)\eta_y = 0$$

$$(K_{123}+K_y)D_y^2\eta_y + K_1 D_x^2\eta_y + \tilde{\alpha}_y(T)\eta_y + (K_2 D_x D_y + K_3 D_y D_x)\eta_x + iw(M+H)\eta_x = 0 \qquad \text{(A.9)}$$

where we have denoted $K_{123} \equiv K_1 + K_2 + K_3$ and

$$\tilde{\alpha}_i(T) = -\alpha_{0i}\left(\frac{T_c^{(i)} - T}{T_c^{(i)}}\right) + gM^2, \qquad i = \{x, y\} \qquad \text{(A.10)}$$

denotes the renormalized quadratic coefficients in the GL expansion due to the effect of coupling to the internal magnetization. Note that generically, the two transition temperatures T_c^x and T_c^y are not necessarily equal to each other, although the quartic coupling between the components of $\boldsymbol{\eta}$ means that in an experiment, both components become non-zero below the same physical T_c.

Unfortunately, the coupled differential equations (A.9) do not admit an analytical solution. Some progress can be made by searching for the solution in the form

$$\eta_i(x, y, z) \sim \tilde{\eta}(y) e^{ik_x d} e^{ik_z b}, \qquad \text{(A.11)}$$

and ignoring the derivatives ∂_x in the Eqs. (A.9). Then, the equations simplify:

$$-K_1\partial_y^2\eta_x(y) + (K_{123}+K_x)\left(\frac{2\pi H}{\Phi_0}\right)^2 y^2\eta_x(y) \quad +\tilde{\alpha}_x(T)\eta_x - iw(M+H)\eta_y = 0 \qquad \text{(A.12)}$$

$$-(K_{123}+K_y)\partial_y^2\eta_y(y) + K_1\left(\frac{2\pi H}{\Phi_0}\right)^2 y^2\eta_y(y) \quad +\tilde{\alpha}_y(T)\eta_y + iw(M+H)\eta_x = 0 \qquad \text{(A.13)}$$

In order to allow for an analytical solution, let us limit the discussion to the case when

$w = 0$ (i.e. the case of a unitary order parameter). Then, it is straightforward to find the solution for the upper critical field similar to the procedure in the main text:

$$\begin{aligned} H_{c2}^{(x)} &= \frac{\Phi_0}{2\pi\sqrt{K_1(K_{123}+K_x)}}\left[\alpha_{0x}\left(\frac{T_c^x - T}{T_c^x}\right) - gM^2(H)\right] \\ H_{c2}^{(y)} &= \frac{\Phi_0}{2\pi\sqrt{K_1(K_{123}+K_y)}}\left[\alpha_{0y}\left(\frac{T_c^y - T}{T_c^y}\right) - gM^2(H)\right]. \end{aligned} \tag{A.14}$$

Without carrying out the detailed calculation, which would depend on the phenomenological parameters of the GL theory and the details of the $M(H)$ dependence, it is clear that the H_{c2} is reduced for both components of the order parameter because of the presence of magnetization (g is positive in the free energy Eq. (A.7)). In particular, when $M(H)$ undergoes a metamagentic transition at field H^* as in UTe$_2$, the magnetization suddenly increases, and this has the potential of significantly reducing H_{c2}. We conclude that the behavior is qualitatively the same as described in the main text.

The physical H_{c2} is the larger of the two expressions in Eq. (A.14) above, and we further argue that $H_{c2}^x > H_{c2}^y$ in UTe$_2$. Indeed, using the effective mass approximation to the electron dispersion Eq. (7) in the main text, we conclude that $K_x \sim t_c d^2/\hbar^2$ is proportional to the interlayer hopping strength t_c. That hopping is presumably very small due to the quasi-2D nature of the Fermi surfaces of UTe$_2$, as remarked in the main text, and hence $K_x \ll K_y$, making $H_{c2}^x > H_{c2}^y$ in the limit of zero temperature, where we can neglect the difference between α_x and α_y. This is entirely consistent with the presence of two superconducting regions, denoted “SC1” and “SC2” in Figs. 3 and 4 in the main text, with SC1 having a higher H_{c2}. In our notation,

$$\text{SC1 :} \qquad \boldsymbol{\eta}_1 \sim (1,0) \propto B_{3u} \tag{A.15}$$

$$\text{SC2 :} \qquad \boldsymbol{\eta}_2 \sim (1,\delta) \text{ or } (1,i\delta) \propto B_{3u} + B_{1u} \tag{A.16}$$

Bibliography

[1] H Kamerlingh Onnes. Further experiments with liquid helium. C. on the change of electric resistance of pure metals at very low temperatures etc. IV. the resistance of pure mercury at helium temperatures. In Through Measurement to Knowledge: The Selected Papers of Heike Kamerlingh Onnes 1853–1926, pages 261–263. Springer, 1991.

[2] Walther Meissner and Robert Ochsenfeld. Ein neuer effekt bei eintritt der supraleitfähigkeit. Naturwissenschaften, 21(44):787–788, 1933.

[3] Fritz London and Heinz London. The electromagnetic equations of the superconductor. Proceedings of the Royal Society of London. Series A-Mathematical and Physical Sciences, 149(866):71–88, 1935.

[4] VL Ginzburg. Zh. vl ginzburg and ld landau. Zh. Eksp. Teor. Fiz, 20:1064, 1950.

[5] Alexei Alexeyevich Abrikosov. The magnetic properties of superconducting alloys. Journal of Physics and Chemistry of Solids, 2(3):199–208, 1957.

[6] J. Bardeen, L. N. Cooper, and J. R. Schrieffer. Microscopic theory of superconductivity. Phys. Rev., 106:162–164, Apr 1957.

[7] E. Helfand and N. R. Werthamer. Temperature and purity dependence of the superconducting critical field, H_{c2}. II. Phys. Rev., 147:288–294, Jul 1966.

[8] N. R. Werthamer E. Helfand. Temperature and purity dependence of the superconducting critical field, $\mathrm{H}_{\mathrm{c}2}$. III. electron spin and spin-orbit effects. Physical Review, 147(1):295–302, 1966.

[9] Kazumi Maki. The magnetic properties of superconducting alloys. II. Physics Physique Fizika, 1(2):127, 1964.

[10] Dai Aoki, Andrew Huxley, Eric Ressouche, Daniel Braithwaite, Jacques Flouquet, Jean-Pascal Brison, Elsa Lhotel, and Carley Paulsen. Coexistence of superconductivity and ferromagnetism in URhGe. Nature, 413(6856):613–616, Oct 2001.

[11] NT Huy, A Gasparini, DE De Nijs, Y Huang, JCP Klaasse, T Gortenmulder, Anne de Visser, A Hamann, T Görlach, and H v Löhneysen. Superconductivity on the border of weak itinerant ferromagnetism in UCoGe. Physical review letters, 99(6):067006, 2007.

[12] Dai Aoki, Kenji Ishida, and Jacques Flouquet. Review of u-based ferromagnetic superconductors: Comparison between UGe_2, URhGe, and UCoGe. Journal of the Physical Society of Japan, 88(2):022001, 2019.

[13] Dai Aoki and Jacques Flouquet. Ferromagnetism and superconductivity in uranium compounds. Journal of the Physical Society of Japan, 81(1):011003, 2011.

[14] T. Hattori, Y. Ihara, Y. Nakai, K. Ishida, Y. Tada, S. Fujimoto, N. Kawakami, E. Osaki, K. Deguchi, N. K. Sato, and I. Satoh. Superconductivity induced by longitudinal ferromagnetic fluctuations in UCoGe. Phys. Rev. Lett., 108:066403, Feb 2012.

[15] Y. Noma, H. Kotegawa, T. Kubo, H. Tou, H. Harima, Y. Haga, E. Yamamoto, Y. Ōnuki, K.M. Itoh, E.E. Haller, A. Nakamura, Y. Homma, F. Honda, and D. Aoki. 73Ge-NMR study on magnetic fluctuations of ferromagnetic superconductor UGe_2. Physica B: Condensed Matter, 536:543–545, 2018.

[16] I Sheikin, A Huxley, Daniel Braithwaite, JP Brison, S Watanabe, K Miyake, and Jacques Flouquet. Anisotropy and pressure dependence of the upper critical field of the ferromagnetic superconductor UGe_2. Physical Review B, 64(22):220503, 2001.

[17] F Lévy, I Sheikin, B Grenier, and Andrew D Huxley. Magnetic field-induced superconductivity in the ferromagnet URhGe. Science, 309(5739):1343–1346, 2005.

[18] Dai Aoki, Tatsuma D. Matsuda, Valentin Taufour, Elena Hassinger, Georg Knebel, and Jacques Flouquet. Extremely large and anisotropic upper critical field and the ferromagnetic instability in UCoGe. Journal of the Physical Society of Japan, 78(11):113709, 2009.

[19] Sheng Ran, Chris Eckberg, Qing-Ping Ding, Yuji Furukawa, Tristin Metz, Shanta R Saha, I-Lin Liu, Mark Zic, Hyunsoo Kim, Johnpierre Paglione, et al. Nearly ferromagnetic spin-triplet superconductivity. Science, 365(6454):684–687, 2019.

[20] Dai Aoki, Jean-Pascal Brison, Jacques Flouquet, Kenji Ishida, Georg Knebel, Y Tokunaga, and Youichi Yanase. Unconventional superconductivity in UTe_2. Journal of Physics: Condensed Matter, 34(24):243002, 2022.

[21] Dai Aoki, Ai Nakamura, Fuminori Honda, DeXin Li, Yoshiya Homma, Yusei Shimizu, Yoshiki J Sato, Georg Knebel, Jean-Pascal Brison, Alexandre Pourret, et al. Unconventional superconductivity in heavy fermion UTe_2. Journal of the Physical Society of Japan, 88(4):043702, 2019.

[22] Sheng Ran, I-Lin Liu, Yun Suk Eo, Daniel J Campbell, Paul M Neves, Wesley T Fuhrman, Shanta R Saha, Christopher Eckberg, Hyunsoo Kim, David Graf, et al. Extreme magnetic field-boosted superconductivity. Nature Physics, pages 1–5, 2019.

[23] Dai Aoki, Fuminori Honda, Georg Knebel, Daniel Braithwaite, Ai Nakamura, DeXin Li, Yoshiya Homma, Yusei Shimizu, Yoshiki J Sato, Jean-Pascal Brison, et al. Multiple superconducting phases and unusual enhancement of the upper critical field in UTe_2. journal of the physical society of japan, 89(5):053705, 2020.

[24] Wen-Chen Lin, Daniel J Campbell, Sheng Ran, I-Lin Liu, Hyunsoo Kim, Andriy H Nevidomskyy, David Graf, Nicholas P Butch, and Johnpierre Paglione. Tuning magnetic confinement of spin-triplet superconductivity. npj Quantum Materials, 5(1):68, 2020.

[25] Sheng Ran, Shanta R Saha, I-Lin Liu, David Graf, Johnpierre Paglione, and Nicholas P Butch. Expansion of the high field-boosted superconductivity in UTe_2 under pressure. npj Quantum Materials, 6(1):75, 2021.

[26] Genki Nakamine, Shunsaku Kitagawa, Kenji Ishida, Yo Tokunaga, Hironori Sakai, Shinsaku Kambe, Ai Nakamura, Yusei Shimizu, Yoshiya Homma, Dexin Li, Fuminori Honda, and Dai Aoki. Superconducting properties of heavy fermion UTe_2 revealed by 125Te-nuclear magnetic resonance. Journal of the Physical Society of Japan, 88(11):113703, 2019.

[27] Genki Nakamine, Katsuki Kinjo, Shunsaku Kitagawa, Kenji Ishida, Yo Tokunaga, Hironori Sakai, Shinsaku Kambe, Ai Nakamura, Yusei Shimizu, Yoshiya Homma, et al. Anisotropic response of spin susceptibility in the superconducting state of UTe_2 probed with Te 125-NMR measurement. Physical Review B, 103(10):L100503, 2021.

[28] Frank Wilczek. Majorana returns. Nature Physics, 5(9):614–618, Sep 2009.

[29] N. Read and Dmitry Green. Paired states of fermions in two dimensions with breaking of parity and time-reversal symmetries and the fractional quantum Hall effect. Phys. Rev. B, 61:10267–10297, Apr 2000.

[30] Tristin Metz, Seokjin Bae, Sheng Ran, I-Lin Liu, Yun Suk Eo, Wesley T. Fuhrman, Daniel F. Agterberg, Steven M. Anlage, Nicholas P. Butch, and Johnpierre Paglione. Point-node gap structure of the spin-triplet superconductor ute_2. Phys. Rev. B, 100:220504, Dec 2019.

[31] Seokjin Bae, Hyunsoo Kim, Sheng Ran, Yun Suk Eo, I-Lin Liu, Wesley Fuhrman, Johnpierre Paglione, Nicholas P Butch, and Steven Anlage. Anomalous normal fluid response in a chiral superconductor, 2019.

[32] Ian M. Hayes, Di S. Wei, Tristin Metz, Jian Zhang, Yun Suk Eo, Sheng Ran, Shanta R. Saha, John Collini, Nicholas P. Butch, Daniel F. Agterberg, Aharon Kapitulnik, and Johnpierre Paglione. Weyl superconductivity in UTe_2, 2020.

[33] Lin Jiao, Sean Howard, Sheng Ran, Zhenyu Wang, Jorge Olivares Rodriguez, Manfred Sigrist, Ziqiang Wang, Nicholas P. Butch, and Vidya Madhavan. Chiral superconductivity in heavy-fermion metal UTe_2. Nature, 579(7800):523–527, Mar 2020.

[34] Catherine Kallin. Chiral p-wave order in Sr2RuO4. Reports on Progress in Physics, 75(4):042501, 2012.

[35] Ying Xing, He Wang, Chao-Kai Li, Xiao Zhang, Jun Liu, Yangwei Zhang, Jiawei Luo, Ziqiao Wang, Yong Wang, Langsheng Ling, Mingliang Tian, Shuang Jia, Ji Feng, Xiong-Jun Liu, Jian Wei, and Jian Wang. Superconductivity in topologically nontrivial material Au_2Pb. npj Quantum Materials, 1(1):16005, Jul 2016.

[36] Ying Xing, Zhibin Shao, Jun Ge, Jiawei Luo, Jinhua Wang, Zengwei Zhu, Jun Liu, Yong Wang, Zhiying Zhao, Jiaqiang Yan, David Mandrus, Binghai Yan, Xiong-Jun Liu, Minghu Pan, and Jian Wang. Surface superconductivity in the type II Weyl semimetal $TaIrTe_4$. National Science Review, 7(3):579–587, 12 2019.

[37] Di S Wei, David Saykin, Oliver Y Miller, Sheng Ran, Shanta R Saha, Daniel F Agterberg, Jörg Schmalian, Nicholas P Butch, Johnpierre Paglione, and Aharon Kapitulnik. Interplay between magnetism and superconductivity in UTe_2. Physical Review B, 105(2):024521, 2022.

[38] Nicholas P Butch, Sheng Ran, Shanta R Saha, Paul M Neves, Mark P Zic, Johnpierre Paglione, Sergiy Gladchenko, Qiang Ye, and Jose A Rodriguez-Rivera. Symmetry of magnetic correlations in spin-triplet superconductor UTe_2. npj Quantum Materials, 7(1):39, 2022.

[39] Lin Miao, Shouzheng Liu, Yishuai Xu, Erica C Kotta, Chang-Jong Kang, Sheng Ran, Johnpierre Paglione, Gabriel Kotliar, Nicholas P Butch, Jonathan D Denlinger, et al. Low energy band structure and symmetries of UTe_2 from angle-resolved photoemission spectroscopy. Physical review letters, 124(7):076401, 2020.

[40] Yuanji Xu, Yutao Sheng, and Yi-feng Yang. Quasi-two-dimensional fermi surfaces and unitary spin-triplet pairing in the heavy fermion superconductor UTe_2. Physical review letters, 123(21):217002, 2019.

[41] Jun Ishizuka, Shuntaro Sumita, Akito Daido, and Youichi Yanase. Insulator-metal transition and topological superconductivity in UTe_2 from a first-principles calculation. Physical Review Letters, 123(21):217001, 2019.

[42] AG Lebed and K Yamaji. Restoration of superconductivity in high parallel magnetic fields in layered superconductors. Physical review letters, 80(12):2697, 1998.

[43] Andrei G Lebed. Restoration of superconductivity in high magnetic fields in UTe_2. Modern Physics Letters B, 34(32):2030007, 2020.

[44] Craig T Van Degrift. Tunnel diode oscillator for 0.001 ppm measurements at low temperatures. Review of Scientific Instruments, 46(5):599–607, 1975.

[45] B. van der Pol. The nonlinear theory of electric oscillations. Proceedings of the Institute of Radio Engineers, 22(9):1051–1086, 1934.

[46] RB Clover and WP Wolf. Magnetic susceptibility measurements with a tunnel diode oscillator. Review of Scientific Instruments, 41(5):617–621, 1970.

[47] MD Vannette, AS Sefat, S Jia, SA Law, G Lapertot, SL Bud'ko, PC Canfield, J Schmalian, and R Prozorov. Precise measurements of radio-frequency magnetic susceptibility in ferromagnetic and antiferromagnetic materials. Journal of Magnetism and Magnetic Materials, 320(3-4):354–363, 2008.

[48] Ruslan Prozorov, Matthew D Vannette, German D Samolyuk, Stephanie A Law, Sergey L Bud'ko, and Paul C Canfield. Contactless measurements of shubnikov-de haas oscillations in the magnetically ordered state of $CeAgSb_2$ and $SmAgSb_2$ single crystals. Physical Review B, 75(1):014413, 2007.

[49] Yogesh Singh, C Martin, SL Bud'Ko, A Ellern, R Prozorov, and DC Johnston. Multigap superconductivity and shubnikov–de haas oscillations in single crystals of the layered boride OsB_2. Physical Review B, 82(14):144532, 2010.

[50] Yogesh Singh, A Niazi, MD Vannette, R Prozorov, and DC Johnston. Superconducting and normal-state properties of the layered boride OsB_2. Physical Review B, 76(21):214510, 2007.

[51] R Prozorov and RW Giannetta. Superconductor science and technology 19. R41, 2006.

[52] H Kim, NH Sung, BK Cho, MA Tanatar, and R Prozorov. Magnetic penetration depth in single crystals of $SrPd_2$ Ge_2 superconductor. Physical Review B, 87(9):094515, 2013.

[53] Hyunsoo Kim, Makariy A Tanatar, and Ruslan Prozorov. Tunnel diode resonator for precision magnetic susceptibility measurements in a mk temperature range and large dc magnetic fields. Review of Scientific Instruments, 89(9):094704, 2018.

[54] V. P. Mineev. Reentrant superconductivity in URhGe. Phys. Rev. B, 91:014506, Jan 2015.

[55] Shyam Sundar, S Gheidi, K Akintola, AM Côté, SR Dunsiger, S Ran, NP Butch, SR Saha, J Paglione, and JE Sonier. Coexistence of ferromagnetic fluctuations and superconductivity in the actinide superconductor UTe_2. Physical Review B, 100(14):140502, 2019.

[56] Lin Jiao, Zhenyu Wang, Sheng Ran, Jorge Olivares Rodriguez, Manfred Sigrist, Ziqiang Wang, Nicholas Butch, and Vidya Madhavan. Microscopic evidence for a chiral superconducting order parameter in the heavy fermion superconductor UTe_2, 2019.

[57] Georg Knebel, William Knafo, Alexandre Pourret, Qun Niu, Michal Vališka, Daniel Braithwaite, Gérard Lapertot, Marc Nardone, Abdelaziz Zitouni, Sanu Mishra, Ilya Sheikin, Gabriel Seyfarth, Jean-Pascal Brison, Dai Aoki, and Jacques Flouquet. Field-reentrant superconductivity close to a metamagnetic transition in the heavy-fermion superconductor UTe_2. Journal of the Physical Society of Japan, 88(6):063707, 2019.

[58] Sheng Ran, Hyunsoo Kim, I-Lin Liu, Shanta Saha, Ian Hayes, Tristin Metz, Yun Suk Eo, Johnpierre Paglione, and Nicholas P. Butch. Enhanced spin triplet superconductivity due to kondo destabilization, 2019.

[59] D. Braithwaite, M. Valiska, G. Knebel, G. Lapertot, J.-P. Brison, A. Pourret, M. E. Zhitomirsky, J. Flouquet, F. Honda, and D. Aoki. Multiple superconducting phases in a nearly ferromagnetic system. Communications Physics, 2(1):147, 2019.

[60] William Knafo, Michal Vališka, Daniel Braithwaite, Gérard Lapertot, Georg Knebel, Alexandre Pourret, Jean-Pascal Brison, Jacques Flouquet, and Dai Aoki. Magnetic-field-induced phenomena in the paramagnetic superconductor UTe_2. Journal of the Physical Society of Japan, 88(6):063705, 2019.

[61] Atsushi Miyake, Yusei Shimizu, Yoshiki J. Sato, Dexin Li, Ai Nakamura, Yoshiya Homma, Fuminori Honda, Jacques Flouquet, Masashi Tokunaga, and Dai Aoki. Metamagnetic transition in heavy fermion superconductor UTe_2. Journal of the Physical Society of Japan, 88(6):063706, 2019.

[62] Ge J Piermarini, S Block, JD Barnett, and RA Forman. Calibration of the pressure dependence of the R 1 ruby fluorescence line to 195 kbar. Journal of Applied Physics, 46(6):2774–2780, 1975.

[63] Deirdre D Ragan, R Gustavsen, and David Schiferl. Calibration of the ruby R 1 and R 2 fluorescence shifts as a function of temperature from 0 to 600 K. Journal of applied physics, 72(12):5539–5544, 1992.

[64] H. Kim, N. H. Sung, B. K. Cho, M. A. Tanatar, and R. Prozorov. Magnetic penetration depth in single crystals of $SrPd_2Ge_2$ superconductor. Phys. Rev. B, 87:094515, Mar 2013.

[65] K. Cho, H. Kim, M. A. Tanatar, Y. J. Song, Y. S. Kwon, W. A. Coniglio, C. C. Agosta, A. Gurevich, and R. Prozorov. Anisotropic upper critical field and possible fulde-ferrel-larkin-ovchinnikov state in the stoichiometric pnictide superconductor LiFeAs. Phys. Rev. B, 83:060502, Feb 2011.

[66] Plengchart Prommapan, Makariy A Tanatar, Bumsung Lee, Seunghyun Khim, Kee Hoon Kim, and Ruslan Prozorov. Magnetic-field-dependent pinning potential in LiFeAs superconductor from its campbell penetration depth. Physical Review B, 84(6):060509, 2011.

[67] A. H. Nevidomskyy. Stability of a nonunitary triplet pairing on the border of magnetism in UTe_2, 2020.

[68] V. P. Mineev and K. V. Samokhin. Introduction to Unconventional Superconductivity. CRC Press, 1999.

[69] M. Tinkham. Introduction to Superconductivity. Dover publications, 2004.

[70] N. R. Werthamer, E. Helfand, and P. C. Hohenberg. Temperature and purity dependence of the superconducting critical field, H_{c2}. III. Electron spin and spin-orbit effects. Physical Review, 147(1):295–302, 1966.

[71] Lin Miao, Shouzheng Liu, Yishuai Xu, Erica Kotta, Chang-Jong Kang, Sheng Ran, Johnpierre Paglione, Gabriel Kotliar, Nicholas P. Butch, Jonathan D. Denlinger, and L. Andrew Wray. Low energy band structure and symmetries of UTe_2 from angle resolved photoemission spectroscopy, 2019.

[72] Vladimir Petrovich Mineev. Reentrant superconductivity in UTe_2. JETP Letters, 111:715–719, 2020.

[73] E. H. Hall. On a new action of the magnet on electric currents. American Journal of Mathematics, 2(3):287–292, 1879.

[74] EH Hall. On the possibility of transverse currents in ferromagnets. Philos. Mag, 12:157–172, 1881.

[75] Naoto Nagaosa, Jairo Sinova, Shigeki Onoda, A. H. MacDonald, and N. P. Ong. Anomalous hall effect. Rev. Mod. Phys., 82:1539–1592, May 2010.

[76] M Hadžić-Leroux, A Hamzić, A Fert, P Haen, F Lapierre, and O Laborde. Hall effect in heavy-fermion systems: UPt_3, UAl_2, $CeAl_3$, $CeRu_2Si_2$. Europhysics Letters, 1(11):579, 1986.

[77] J Schoenes and JJM Franse. Hall effect in the heavy-fermion superconductor UPt_3. Physical Review B, 33(7):5138, 1986.

[78] A Fert and PM Levy. Theory of the hall effect in heavy-fermion compounds. Physical Review B, 36(4):1907, 1987.

[79] Qun Niu, Georg Knebel, Daniel Braithwaite, Dai Aoki, Gérard Lapertot, Michal Vališka, Gabriel Seyfarth, William Knafo, Toni Helm, J-P Brison, et al. Evidence of fermi surface reconstruction at the metamagnetic transition of the strongly correlated superconductor UTe_2. Physical Review Research, 2(3):033179, 2020.

[80] Tian Liang, Jingjing Lin, Quinn Gibson, Satya Kushwaha, Minhao Liu, Wudi Wang, Hongyu Xiong, Jonathan A Sobota, Makoto Hashimoto, Patrick S Kirchmann, et al. Anomalous hall effect in $ZrTe_5$. Nature Physics, 14(5):451–455, 2018.

[81] Jiadong Zhou, Wenjie Zhang, Yung-Chang Lin, Jin Cao, Yao Zhou, Wei Jiang, Huifang Du, Bijun Tang, Jia Shi, Bingyan Jiang, et al. Heterodimensional superlattice with in-plane anomalous Hall effect. Nature, 609(7925):46–51, 2022.

[82] Hui Wang, Yue-Xin Huang, Huiying Liu, Xiaolong Feng, Jiaojiao Zhu, Weikang Wu, Cong Xiao, and Shengyuan A Yang. Theory of intrinsic in-plane Hall effect. arXiv preprint arXiv:2211.05978, 2022.

[83] Colman Goldberg and RE Davis. New galvanomagnetic effect. Physical Review, 94(5):1121, 1954.

[84] Vladimir A Zyuzin. In-plane Hall effect in two-dimensional helical electron systems. Physical Review B, 102(24):241105, 2020.

[85] Raffaele Battilomo, Niccoló Scopigno, and Carmine Ortix. Anomalous planar Hall effect in two-dimensional trigonal crystals. Physical Review Research, 3(1):L012006, 2021.

[86] James H Cullen, Pankaj Bhalla, Elizabeth Marcellina, Alexander R Hamilton, and Dimitrie Culcer. Generating a topological anomalous Hall effect in a nonmagnetic conductor: An in-plane magnetic field as a direct probe of the Berry curvature. Physical Review Letters, 126(25):256601, 2021.

[87] Hiroshi Kontani and Kosaku Yamada. Theory of anomalous Hall effect in heavy fermion system. Journal of the Physical Society of Japan, 63(7):2627–2652, 1994.

[88] Yun Suk Eo, Shouzheng Liu, Shanta R Saha, Hyunsoo Kim, Sheng Ran, Jarryd A Horn, Halyna Hodovanets, John Collini, Tristin Metz, Wesley T Fuhrman, et al. c-axis transport in UTe_2: Evidence of three-dimensional conductivity component. Physical Review B, 106(6):L060505, 2022.

[89] Takashi Kurumaji. Symmetry-based requirement for the measurement of electrical and thermal Hall conductivity under an in-plane magnetic field. arXiv preprint arXiv:2304.00785, 2023.

[90] Xin Liu, Hsiu-Chuan Hsu, and Chao-Xing Liu. In-plane magnetization-induced quantum anomalous Hall effect. Physical review letters, 111(8):086802, 2013.

[91] Jun Ishizuka, Shuntaro Sumita, Akito Daido, and Youichi Yanase. Insulator-Metal Transition and Topological Superconductivity in UTe_2 from a First-Principles Calculation. Phys. Rev. Lett., 123(21):217001, November 2019.